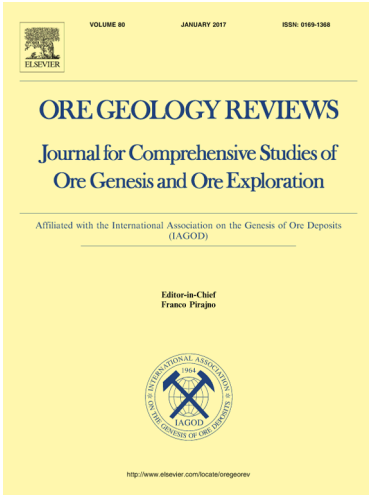

Multiphase magma intrusion, ore-enhancement and hydrothermal carbonatisation in the Siah-Kamar porphyry Mo deposit, Urumieh-Dokhtar magmatic zone, NW Iran

Ahmad Rabiee, Federico Rossetti, Francesca Tecce, Yoshihiro Asahara, Hossein Azizi, Johannes Glodny, Federico Lucci, Reza Nozaem, Joachim Opitz, David Selby

PII: S0169-1368(19)30160-X
DOI: https://doi.org/10.1016/j.oregeorev.2019.05.016
Reference: OREGEO 2930

To appear in: *Ore Geology Reviews*

Received Date: 22 February 2019
Revised Date: 8 May 2019
Accepted Date: 13 May 2019

Please cite this article as: A. Rabiee, F. Rossetti, F. Tecce, Y. Asahara, H. Azizi, J. Glodny, F. Lucci, R. Nozaem, J. Opitz, D. Selby, Multiphase magma intrusion, ore-enhancement and hydrothermal carbonatisation in the Siah-Kamar porphyry Mo deposit, Urumieh-Dokhtar magmatic zone, NW Iran, *Ore Geology Reviews* (2019), doi: https://doi.org/10.1016/j.oregeorev.2019.05.016

Multiphase magma intrusion, ore-enhancement and hydrothermal carbonatisation in the Siah-Kamar porphyry Mo deposit, Urumieh-Dokhtar magmatic zone, NW Iran

Ahmad Rabiee[1], Federico Rossetti[1,*], Francesca Tecce[2], Yoshihiro Asahara[3], Hossein Azizi[4], Johannes Glodny[5], Federico Lucci[1], Reza Nozaem[6], Joachim Opitz[7], David Selby[8,9]

[1] *Dipartimento di Scienze, Università degli Studi Roma Tre, Roma, Italy*
[2] *Istituto di Geologia Ambientale e Geoingegneria, CNR, Rome, Italy*
[3] *Department of Earth and Environmental Sciences, Nagoya University, Nagoya, Japan*
[4] *Mining Department, Faculty of Engineering, University of Kurdistan, Sanandaj, Iran.*
[5] *GFZ German Research Centre for Geosciences, Potsdam, Germany*
[6] *School of Geology, University of Tehran, Tehran, Iran*
[7] *Institut für Mineralogie und Kristallchemie, Universität Stuttgart, Stuttgart, Germany*
[8] *Department of Earth Sciences, Durham University, Durham, UK*
[9] *State Key Laboratory of Geological Processes and Mineral Resources, School of Earth Resources, China University of Geosciences, Wuhan, China*

*Corresponding Author:
Dipartimento di Scienze
Sezione di Scienze Geologiche
Università Roma Tre
Largo S. L. Murialdo, 1
00146 Roma (ITALY)
Phone: +390657338043
FAX: +390657338201
e-mail: federico.rossetti@uniroma3.it
Skype: fede.rossetti

Abstract

The Siah-Kamar Mo deposit (SKMD) is located at the northwestern termination of the Urumieh-Dokhtar magmatic zone and it is the only porphyry Mo ore reserve in Iran. The exploration program documented 39.2 Mt proved reserves @ 539 ppm Mo and 66.4 Mt probable reserves @ 266 ppm Mo. In this study, field and petrographic investigations, integrated with geochemical (fluid inclusion and quartz chemistry) and geochronological (U-Pb zircon, Re-Os molybdenite, and Rb-Sr multimineral isochron) studies are used to propose a metallogenic model for the Mo mineralisation in the SKMD. The geology of the SKMD is characterized by the emplacement of a multiphase Oligocene basic/intermediate (at ca. 33-30 Ma) to acidic (29-28 Ma) magmatic suite, which intruded the Eocene volcanic country rocks. The alteration zone, about 4 × 3 km in size and with a general NW-SE trend, is centered within the main basic porphyry stock, grading from an inner potassic-sodic zone to peripheral phyllic/propylitic halos. The late acidic magmatic products (stocks and dykes) intruded and post-dated the main alteration zone. Two-stage Mo mineralisation is recognised, including: (i) stage-1, disseminated molybdenite, coeval with the formation of potassic-sodic alteration and minor, microscale Fsp, Bt, Qz+Po veinlets; and (ii) stage-2, high-grade molybdenite+carbonate (± sericite), structurally-controlled stockwork veining. Fluid inclusion systematics combined with TitaniQ thermometry documents a mineralising fluid system compatible with a transition from high-temperature (up to ca. 600 °C) magmatic to epithermal (250 °C) conditions during progressive cooling, exhumation and mixing with meteoric sources at shallow crustal conditions (ca. 7-3 km). The Re-Os molybdenite dating constrains the high-grade Mo ore formation at ca. 29-28 Ma, attesting for the intimate linkage between the main Mo mineralisation and the acidic magmatic phase in the area. The Rb-Sr geochronology of the potassic-sodic alteration zones confirms the two-stage magmatic/mineralisation scenarios, overlapping within errors with the results obtained from the U-Pb zircon geochronology and constraining the formation of the potassic-sodic and phyllic alteration at ca. 33 and 28 Ma, respectively. Our results document an uncommon scenario of two-stage porphyry Mo mineralisation associated with intensive late stage carbonate precipitation and achieved during a long-lasting and multiphase magmatic pulses of Oligocene age. We highlight the dominant role of acidic fluid neutralisation for further ore enrichment during polyphase magma intrusion as the dominant factor controlling the Mo mineralisation in the SKMD. Comparison at a regional-scale indicates that parameters such as longevity of magma supply, progressive magma crystallization/differentiation, and the

presence of a possible pre-enriched crustal material should be considered responsible for the Mo endowment in the UDMZ.

Key words: porphyry Mo, ore deposits, magmatism, fluids, Urumieh-Dokhtar zone, Iran

1. Introduction

Molybdenum (Mo) porphyry-type deposits supply the main Mo demands worldwide (> 95%) (John and Taylor, 2016). The Mo deposits are mainly associated with subduction-related settings, such as volcano-plutonic magmatic arcs, back-arcs and continental collision orogens (Westra and Keith, 1981; Wallace, 1995; Seedorff et al., 2005; Taylor et al., 2012; Wu et al., 2017). They are mainly located in the western Cordillera of North America (Ayres et al., 1982; Duke, 2007; Kerr et al., 2009), in Eastern Europe (Janković, 1982), Australia (Whitcher, 1975), China (Mao et al., 2008; Zeng et al., 2012; Wu et al., 2017), Russia (Sutulov, 1973), and elsewhere in Asia (Heinhorst et al., 2000).

Porphyry molybdenum deposits have been classified based on the Mo modal abundance, F content, geochemical fingerprint of associated magmatism, and geodynamic setting of formation (Westra and Keith, 1981; Ludington et al., 2009; Ludington and Plumlee, 2009; Taylor et al., 2012; Wu et al., 2017). In particular, two end-member porphyry Mo mineralisation types have been proposed in the literature: the Endako- and the Climax-type (Selby and Creaser, 2001). The Endako-type deposits are characterised by low-grade (Mo<0.15 wt.%), but large-tonnage Mo ores and low F (<0.05 wt.%) in a continental arc setting associated with calc-alkaline magmatism. Tungsten may be enriched as a by-product metal, but copper occurs as in minor quantities or is absent (Doebrich et al., 1996; Taylor et al., 2012). The Climax-type deposits are instead characterised by high-grade (Mo>0.15 wt.%) Mo ores and high F (>0.05 wt.%) in an intraplate setting and associated with alkali-calcic and alkali magmatism (Westra and Keith, 1981).

The duration of the mineralisation process in porphyry systems commonly ranges from 100 k.y. to 1.5 m.y. (Sillitoe, 2010). Based on numerical modelling, Cathles et al. (1997) proposed a lifetime no longer than 800,000 years for a geothermal system of temperatures greater than 200 °C. The long lifetime (> 1 m.y.) of magmatic-hydrothermal activity mainly depends upon volume, emplacement depth, and temperature of magma, conductive and convective cooling, and permeability of the host rocks (Taylor et al., 2012). It is also demonstrated that multiple events of magma intrusion can increase the lifetime of porphyry

copper deposits in excess of 1 m.y. (Chiaradia et al., 2009; John et al., 2010). The inter-mineral intrusive pulses can be either mineralizing or barren and, consequently, can enrich or destroy the former mineralized zones (Sillitoe, 2010). In particular, long-lived magmatism and fractionation, together with fluid exsolution and a change toward more reducing and acid conditions in the mineralising environment are recognised as the key factors for the Mo endowment in the residual melts (e.g., Candela and Holland, 1986; Keith et al., 1986; Blevin and Chappell, 1992; Candela, 1992; Audetat et al., 2008; Seo et al., 2012; Wilkinson, 2013; Zhang et al., 2018).

The majority of the porphyry Cu–(Mo, Au) deposits in Iran occur along the Cenozoic Urumieh-Dokhtar magmatic zone (UDMZ) and the Arasbaran magmatic zone, including the world-class SarCheshmeh, Sungun, and Meiduk deposits (Asadi et al., 2014; Aghazadeh et al., 2015; Richards and Sholeh, 2016) (Fig. 1 and supplementary material #1). The Siah-Kamar Mo deposit (SKMD) (Nabatian et al., 2017b; Simmonds et al., 2019), located at the northwestern termination of the UDMZ, from Mianeh to Hashtroud cities (Figs. 1 and 2), is the only Mo ore reserve in Iran. Despite the presence of some alteration zones, no porphyry deposits or significant mineralisation has been reported in the area before the exploratory studies carried out by National Iranian Copper Industries Company since 2005 (NICICO, 2010). Preliminary exploration on the altered zones has shown a significant Mo-W enrichment, whereas the deposit is barren with respect to Cu and Au. The exploration program held by the owner within the SKMD documented the in-depth mineralisation down to 600 m, with a 39.2 Mt proved reserves @ 539 ppm Mo and 66.4 Mt probable reserves @ 266 ppm Mo (Aria Kansar Samin Co., 2013).

Early research studies focused on the magmatism and mineralisation characteristics of the ore deposit. These studies defined the metaluminous, high-K calc-alkaline to shoshonitic geochemical fingerprint of the magmatism referred to a final stage of Neo-Tethys subduction beneath the Iranian plate (Khaleghi et al., 2013; Nabatian et al., 2017b). These studies also reported low salinity and low-to-moderate temperature magmatic fluids as responsible for the mineralisation (Nabatian et al., 2017b). Contrasting age estimates exist for the timing of the Mo mineralisation at the SKMD and still uncertain is the timing and geological scenario of the Mo mineralisation. Nabatian et al. (2017b) presented molybdenite weighted mean Re-Os age of 41.9 ± 3.6 Ma, whereas Simmonds et al. (2019) reported ages between 28.10 ± 0.15 and 29.06 ± 0.20 Ma using the same geochronological technique. Simmonds et al. (2019) also reported early Oligocene U-Pb zircon ages (32.70 ± 0.40 Ma to 30.90 ± 0.40 Ma) from the

mineralized body, suggesting mineralization has potentially occurred ~1.5 Ma after the crystallization of the porphyry stock. Moreover, key aspects, such as the longevity of the magmatic porphyry system, the hydrothermal-alteration processes, and the structural control on fluid flow and ore mineralisation were poorly considered.

Based on detailed field and petrographic investigations integrated with analytical data (fluid inclusion microthermometry, U-Pb zircon, Re-Os Molybdenite, and Rb-Sr geochronology, quartz geochemistry), this contribution is aimed at (i) defining a genetic model for the Mo mineralisation at the SKMD, and (ii) improving our knowledge of the Cenozoic metallogeny within the UDMZ (Fig 1). Our results document an Oligocene, long-lasting history of magma crystallisation/emplacement/alteration (33-28 Ma), which culminated with Mo stockwork mineralisation at ca. 29-28 Ma. The Mo mineralisation was structurally controlled and caused by ore enhancement during renewed magmatism, which induced metal leaching and deposition in the transition from ductile-to-brittle environments above a cooling and degassing magma. These data are used to propose a genetic mineralisation model for the Mo ore and to discuss implications for the regional ore distribution, and for the Mo mineralisation in porphyry systems in general.

2. Geological Background

The UDMZ (Fig. 1) records prolonged Cenozoic magmatic activity, spanning from the Paleocene to the Quaternary (e.g., Richards et al., 2006; Chiu et al., 2013; Yeganehfar et al., 2013; Heidari et al., 2015; Ahmadian et al., 2016; Heidarzadeh et al., 2017; Hosseini et al., 2017; Sarjoughian and Kananian, 2017; Shahsavari Alavijeh et al., 2017). A main phase of magmatism occurred during the Eocene-Oligocene, synchronous with the magmatic flare-up at regional scale (Stocklin, 1968; Verdel et al., 2011; Chiu et al., 2013; Moghadam et al., 2016).

Based on the mineralisation distribution and types along the UDMZ, a southern and a northern region can be recognised. The southern region, also known as the Kerman Belt, extending from the Naeen city to Bazman volcano (Naeen-Bazman volcanic zone, NBMZ in Fig. 1), hosts the dominant and largest porphyry Cu-Mo deposits of Iran, which are mostly Miocene in age (Aghazadeh et al., 2015). Magmatic products show a general calc-alkaline (moderate to high-K) and metaluminous fingerprint, with a pronounced adakitic signature during the Miocene (Shahabpour and Kramers, 1987; Hassanzadeh, 1993; Shafiei et al., 2008; Taghipour et al., 2008; Shafiei et al., 2009; Mirnejad et al., 2011; Asadi et al., 2014).

Three metallogenic stages have been proposed by Aghazadeh et al. (2015) within this segment, including late Oligocene (29–27 Ma), middle Miocene (14–11 Ma), and late Miocene (9–6 Ma). The northern region, extending from Urumieh/BostanAbad to Naeen/Anarak cities (Fig. 1; supplementary material #1), instead hosts a few relatively smaller deposits. Within this region, two magmatic zones can be recognised: (i) a volcano-plutonic zone from BostanAbad to Anarak cities (BAMZ in Fig. 1; supplementary material #1), Eocene to Oligocene in age, typified by high-K calc-alkaline and shoshonitic signatures (e.g., granitoid batholiths of Zanjan, Hassanzadeh et al., 2008; Kal-e kafi, Ahmadian et al., 2009; Abhar, Castro et al., 2013; Kuh-e Dom, Sarjoughian and Kananian, 2017) and associated with some small, intrusion-related, polymetallic deposits (Ahmadian et al., 2009; Fazel et al., 2015; Ahmadian et al., 2016); and (ii) an Oligocene-Miocene volcano-plutonic zone from Urumieh to Naeen (UNMZ; in Fig. 1), which is characterized by post-collisional calc-alkaline and high-K calc-alkaline to adakite products (e.g., Richards et al., 2006; Chiu et al., 2013; Yeganehfar et al., 2013; Babazadeh et al., 2017; Ballato et al., 2017b; Sarjoughian and Kananian, 2017) and associated with minor Au-rich Cu (Mo) porphyry (e.g., Dalli, Ayati et al., 2013) and epithermal Au deposits (e.g., Zarshuran, Mehrabi et al., 1999; Muteh, Moritz et al., 2006; SariGunay, Richards et al., 2006). Regarding the Miocene magmatism, Shafiei et al. (2008) suggested syn- and post-collisional thickening and melting of Cu- and sulfur-rich peridotite, near the crust–mantle boundary, as responsible for fertile adakitic magmatism in the southern Urumieh-Dokhtar magmatic zone. In contrast, Haschke et al. (2010) suggested that a syn- or post-collisional Miocene delamination in the northern UDMZ had removed the Cu- and S-enriched metasomatised lithospheric arc-root and, subsequently, prevented the Cu mineralisation during collisional magmatism.

The AMZ is adjacent and sub-parallel to the UDMZ, running from the Sabalan volcano to the Jolfa city, probably continuing to Armenia into the lesser Caucasian Magmatic zone (Innocenti et al., 1982; Hassanpour et al., 2014; Simmonds et al., 2017) (Fig. 1). The AMZ boundaries have not been defined yet, although it is normally considered as a segment of the UDMZ. Nonetheless, it has been also considered as a part of western Alborz zone (Nabavi, 1976; Aghanabati, 2004; Moritz et al., 2016; Rolland, 2017). The porphyry Cu (Mo-Au) mineralisation span from Oligocene to early Miocene (e.g., Shahabpour and Kramers, 1987; McInnes et al., 2003; Aghazadeh et al., 2015) and it is more intense with respect to the northern region of the UDMZ.

3. Materials and Methods

A multidisciplinary research approach is adopted in this study that includes field work and laboratory analyses. Field work was based on the existing 1:250,000 cartography (Amidi et al., 1987) and addressed to map the main magmatic bodies and the alteration types (Fig. 2). A detailed map at the scale 1: 5000 is produced for describing the alteration zoning and the main ore zones (Fig. 3). Field work and petrographical observation form the basis for the sampling strategy for the laboratory work that includes: (i) fluid inclusion microthermometry, (ii) Raman spectroscopy; (iii) LA-ICPMS trace and rare earth (REE) elements analysis; (iv) zircon U-Pb geochronology; (v) molybdenite Re-Os geochronology; and (vi) multi-mineral Rb-Sr geochronology of the alteration assemblages.

The studied samples are shown in Figure 3 and listed in Table 1, where their location, petrography and analytical methods adopted are detailed. The analytical protocols are described in the Appendix. In the following, mineral abbreviations are after Whitney and Evans (2010).

4. Geology of the study area and the ore deposit

The SKMD is located within the Mianeh intermountain basin (Heidarzadeh et al., 2017), in-between the Alborz and the AMZ, at the southern margin of the Azerbaijan Block at the tip of the active dextral Tabriz Fault (Figs. 1, 2). The stratigraphy of the area is dominated by a wide exposure of Eocene volcanic rocks, which make-up the country rocks of the SKMD. The Eocene volcanic rocks consist of andesite-basalt and trachy-andesite lava beds and vitric dacitic to andesitic tuff (Amidi et al., 1987) (Fig. 2). These volcanic products are intruded or covered by a composite Cenozoic (Oligocene-Miocene) volcano-plutonic complex (Amidi et al., 1987; Khodabandeh et al., 1999). A variety of intrusive and sub-volcanic rocks with variable geometry and composition occur in the study area, including diorite, monzonite to leuco-granite, and rhyodacite porphyry (Amidi et al., 1987; Khodabandeh et al., 1999). The granular intrusive bodies crop out in the northwest and centre of the study area, generally aligned along a NW-SE orientation (Fig. 2). To the southeast (from Khatoon Abad to Siah-Kamar), an array of E-W to NE-SW striking microgranular and porphyritic felsic stocks and dykes crop out (Fig. 2). Miocene volcanic country rocks consist of tuff and ash layers with interlayered andesitic lava beds. This volcanic succession is covered by upper Miocene continental sedimentary deposits (Upper Red Fm.) that crop out in the northwestern and southwestern sectors of the study area. These deposits are unconformably covered by

Pliocene-Quaternary continental sedimentary successions (Amidi et al., 1987; Ballato et al., 2017a) (Fig. 2).

The ore deposit geology is characterised by a major alteration zone centered on a porphyry-type, composite magmatic complex that, intruded within the Eocene volcanic rocks, hosts the main Mol ore (Figs. 2 to 4). Despite the different alteration types, the magmatic bodies share common textural features consisting of a porphyritic microgranular and/or glassy groundmass, with various proportions of AFs, Pl, and mafic phenocrysts (Cpx and/or Amp) in the primary igneous assemblage (see Table 1 for a detailed description). Based on the estimated modal abundance of the primary igneous mineral components, the rock compositions are andesitoid/basaltoid (Le Maitre et al., 2005). The mineralized porphyry body (samples MN02 and MN03 in Table 1) is the largest stock in deposit area with a NW-trending ellipsoid shape (1800×1300 m). The body experienced intense alteration and in some places the primary texture has been destroyed. Where preserved, the primary rock composition ranges from syenite to monzonite-quartzmonzonite (Nabatian et al., 2017b). Also barren magmatic bodies can be recognised in the area, to the south (sample MN31 in Table 1) and to the north (sample MN65 in Table 1) of the mineralised body, in a continuum from syn-to-post ore stage as documented by the alteration patterns and distribution (see inset in Fig. 3).

Based on the mapped outcrops of alteration zones and assuming lateral continuity below the Miocene and Pliocene cover rocks, the reconstruction of the alteration zone shows an ellipsoid shape, with a general NW-SE trend and about 4×3 km of areal extent (Fig. 3). The Mol mineralisation occurs both as minor disseminated within the inner potassic-sodic alteration zone and major focused in Qz-Afs-Cb veins.

A suite of acidic subvolcanic products (rhyolitic and dacitoid in composition; samples Mn01 and Mn19 in Table 1) are observed to intrude and post-date the alteration zone. These magmatic rocks show only minor evidence of rock alteration (Fig. 3; Table 1).

5. Alteration types

Alteration zoning grades from potassic-sodic alteration in the centre to adjacent phyllic and peripheral propylitic halos (Fig. 3). In the following, we described the main alteration zones, mineral assemblages and their distribution.

5.1. Potassic-sodic alteration

The potassic-sodic alteration is observed in the core of the altered zone, with an areal extent of ca. 2.4 km^2 (Figs. 3, 4). The alteration is typified by the mineral assemblage Bt+ Kfs + Ab + Mag + Anh ± Ilm, Ap, Mol. Typical is the occurrence of a secondary spotted texture made of Bt-Mag aggregates, likely overprinting early magmatic layering (Fig. 5a). Secondary anhedral Kfs and Ab aggregates overprint early magmatic Pl (Fig. 5b). Molybdenite typically occurs as disseminated flakes within the alteration matrix (Fig. 5c). Biotite occur as very fine grained, dominantly as disseminated grains but also as irregular curvy vein-like aggregates (Fig. 5d). Magnetite grains occur both as fine-grained disseminated crystals in the groundmass and as inclusion in Kfs (Figs. 5b, e). Minor amount of Ilm is observed as inclusions in Bt (Fig. 5e). Late formed Po veins also occur (Figs. 5d). Stockwork development and partial brecciation are ubiquitous and resulted in diverse vein types (Fig. 5a; see also below).

5.2. Propylitic alteration

Propylitic alteration is the largest alteration zone that mainly affects the Eocene volcanic host rocks and the porphyry-type magmatic complex (Figs. 3, 4). The width of the propylitic alteration is at least 1 km, but it suddenly decreases with distance from the porphyry-type magmatic complex. This alteration is typified by the assemblage Ep ± Act ± Cb ± Py with stockwork, disseminated and locally brecciated textures close to the porphyry-type magmatic complex (Fig. 5f).

5.3. Phyllic alteration

The phyllic alteration rims the core of the potassic-sodic and the marginal alteration zone. Locally it overprints the inner part of the potassic alteration zone (Figs. 3, 4). The phyllic alteration consists of the assemblage Qz + Mus + Py, which is variable distributed within the alteration zone, usually associated with veining and rock fractures, seldom associated with intensive pyritization (ca. 5- 10 % vol.). Pyrite is typically altered to secondary iron oxide and hydroxide minerals in the uppermost portions of the alteration zone. Intermediate argillic alteration (Sillitoe, 2010) is observed to decorate the damage zone of major faults (Fig. 5g-j).

6. Veining

We documented multistage veining, locally associated with pronounced alteration halos. The vein density is highly variable and commonly decreases toward margins of the alteration zones, where the alteration distribution is mainly influenced by vein distribution and persistence. In particular, the vein volume abruptly interrupts at the boundary between the mineralised porphyry complex and the Eocene volcanic host rocks (Fig. 6a).

Azimuth rose diagram generated from the measured cumulative vein strikes reveals a mean E-W orientation, associated with minor NW-SE and N-S ones (Fig. 6b). In the following, a description of the vein texture and assemblages is described for each alteration zone.

6.1. Veins in the potassic-sodic alteration zone

A conceptual scheme of the vein generation at the microscale within the inner potassic-sodic zone is presented in Figure 7. The early veins generation (V1) consists of up to mm-size Bt and minor Qz+Po, Ab+Kfs and Kfs veins, sharing a discontinuous and irregular curvy shape. The Fsp veins are commonly associated with Fsp halos; no evidence of Mol mineralisation is observed. Locally, small (up to 0.5 mm) curvy shapes Qz ± Po veins are also observed (Fig. 5d).

The second generation (V2a) consists of a voluminous, cm-sized, Qz-Kfs ± Mol ± Ab non-systematic (stockwork) vein array (Figs. 5a and 8a-c). These veins are characterized by a blocky texture, mainly formed by Qz-Kfs aggregates, commonly associated with minor Mol, Sch, and Rt (Figs. 7 and 8a,c). The overall vein texture suggests syntaxial growth and Mol occurs in equilibrium with Qz (Figs. 7 and 8a,b). Carbonate mineralisation is typified by the early appearance of paraspurite ($Ca_5(SiO_4)_2CO_3$) (Colville and Colville, 1977), and Ank and Sid/Ank in the stage-2 veins, which occurs in the vein suture, likely filling remaining vugs (Fig. 8).

The third generation (V2b) corresponds to the main ore stage and is characterised by Cb-Mol veins, associated with minor sericite and pyrite (Fig. 9). The Cb-Mol veins mostly rework the pre-existing Qz-Fsp veins/host rocks contacts, often developed as cross-cutting and inter-granular cracks (Fig. 9 a,b). Locally, brecciation of the early Qz-Fsp veins is observed, associated with massive Mol precipitation that often show rosette texture (Figs. 9a). A ribbon appearance is commonly observed in the V2b veins due to alternating variation of Cb minerals (Fig. 9c). It is worth nothing that Cb compositions vary from Cal to Sid/Rds/Ank when in equilibrium with the Mol precipitation (Fig. 9b,c). Muscovite mostly developed at the expenses of pristine Kfs (Fig. 9d).

In terms of vein distribution, the overall array of Mol mineralised veins (V2a-V2b) is non-systematic (Fig. 6c). When taking into account the V2b vein array, a more systematic distribution is observed, which cluster along the E-W (dominant) and NS strikes (Fig. 6d).

6.2. Veins in the propylitic alteration zone

The propylitic zone is associated with development of brecciation and veins, close to the porphyry mineralised body and in the distal country rocks, respectively. Brecciation causes

fragmentation of the country rocks, cemented by Ep+Act+Cb aggregates. Veins occur as high-angle systematic arrays, striking roughly E-W and N-S (Fig. 6e), and are filled with the same mineralogical assemblage (Ep+Act+Cb).

6.3. Veins in the phyllic alteration zone

Within the phyllic alteration zone, veins are made of mm-size Qz + Py, associated with sub-mm-size Ms (sericite) halos (Fig. 5g-j). They form non-systematic arrays. Within the higher topographic levels of phyllic alteration, the Py grains are converted to iron oxide and hydroxide minerals.

7. Mo ore mineralisation

Two main stages of Mol mineralisation were recognized either as disseminated or stockwork (Figs. 9 and 10). Stage-1 (Mol-I) occurs as disseminated Mol flakes within the porphyry body, in association with the potassic-sodic alteration (Fig. 5c). Stage-2 can be subdivided in two Mol formation events (stage-2a and -2b in Figs. 9 and 10), Mol-II and Mol-III, respectively. Mol-II occurs during V2a formation, in association with minor Sch and Rt. Mol-III is the high-grade ore stage during the Cb V2b formation, beginning with paraspurite and continuing with Fe-Mn Cb mineralisation. Minor amount of Py and secondary Ms (sericite) are associated with the Mol-III precipitation.

8. Quartz chemistry and Ti-in quartz thermometry

Quartz crystals from V2a veins from the potassic-sodic alteration zone were analyzed by in situ LA-ICP-MS for Ti content (16 grains) and trace elements (7 grains). Results are presented in Table 2 and 3, respectively. Analytical details are provided in the Appendix.

Analyzed quartz show high Ti (17.4-54.7 ppm) and Al (35.9-160.2 ppm), with significant enrichment in Li (1.9-28.0 ppm) and Ge (0.9-2.0 ppm). In the Al vs. Li diagram, the analysed quartz grains show positive correlation and fall near the 1:1 Al/Li molar ratio line, which is indicative of magmatic and hydrothermal quartz (Dennen, 1966; Müller et al., 2018). In the Al vs. Ge diagram, the quartz compositions are compatible with those from hydrothermal quartz and the Ti contents are typical of quartz veins from (Mo-Cu-Au)-porphyry-type deposits (e.g., Müller et al., 2018) (Fig. 11).

The TitaniQ thermometry (Wark and Watson, 2006; revised by Huang and Audétat, 2012), assuming a $aTiO_2 = 1$ for rutile-present conditions provides temperature estimates of 479-575 ± 50 °C and 568-675 ± 50 °C at 0.5 and 2.5 kbar, respectively.

9. Fluid-Inclusion Study

9.1. Petrography

Samples from (i) Qz-Fsp V2a and Cb-Mol V2b veins from the potassic-sodic alteration zone (Fig 9a) and (ii) Qz-Py-Ms veins from the phyllic alteration zone (Fig. 5i) were studied for fluid inclusions (FI) analysis in order to assess the chemical-physical properties of the mineralising fluid(s). FI were measured both in quartz and paraspurite from the same vein assemblage, considered as representative of the main Mol mineralisation stages.

Based on the observed phases at room temperature, two main types of aqueous FI were recognised following the classification proposed by Roedder (1984): (i) dominant type-A (L-rich + V); and (ii) minor, solid-bearing, type-B (L-rich + V + solid). Type-A is subdivided into four sub-groups based on the alteration zone, host mineral and the V to L volume ratio, from A1 to A4. A summary of FI characteristics and results are given in Table 4. The various identified FI types in this study are briefly described below. Type-A1 and A2 are L-rich + V FI, found within V2a quartz grains in the potassic-sodic alteration zone with the V to L ratios from 0.5 to 1 and from 0.1 to 0.4, respectively. Type-A3 are L-rich + V FI. They are the only detected FI inside quartz crystals from Qz+Py+Ser veins within phyllic alteration zone. Type-A4 are L-rich + V FI from V2b paraspurite crystals within the potassic-sodic alteration zone.

Type-A1 are mostly found as solitary or randomly distributed in well-protected Qz grains form post entrapment shearing, and have regular to subhedral geometry, large size (ranging 15-100 μm). They occasionally show negative crystal shape, and possess the highest V to L ratios (Fig 12a). Type-A2 FIs are characterized by small sizes (5 to 20 μm), regular with negative crystal shape to irregular geometry (Fig 12b). Type-A3 are very similar to type-A2 FI, but with smaller sizes (ranging 5 to 10 μm). They have regular to irregular shapes, some showing negative crystal shapes and their V to L ratios range from 0.2 to 0.4 (Fig 12c). Type-A4 occur along the cleavages of the host crystal, showing irregular and elongated geometry with sizes range 5-20 μm. The V to L ratios range from 0.1 to 0.25, but commonly are below 0.15 (Fig 12d).

Type-B are solid-bearing L-rich + V FI, rarely found in the cores of V2a quartz grains (Fig 12e). They occur mainly isolated and in confined trails that are interpreted to be quartz growth lines. Their sizes range 15-30 μm and mostly have irregular geometry. Their V to L ratios range from 0.1 to 0.2.

9.2. Raman Spectroscopy

Raman spectroscopy was utilized to define the composition of V and L phases of the type-A FI. For the types-A1 and A4 FI, the obtained spectra for the L and V phase revealed water and water vapor as the major components, respectively (Fig 13). In addition, the L phase of type-A1 FI also showed a clear peak for CO_2 (at 1384 cm^{-1}) in solution (Fig 13a). Other peaks were too weak and not identified. In the V phase of type-A1 FI, apart from water vapor, the only detected gas component is CO_2 (Fermi doublet at 1285 and 1388 cm^{-1}). A weak peak belonging to CO_3^{2-} (1064 cm^{-1}) was also detected (Fig 13b).

The results from paraspurite-hosted type-A4 FI were not so clear due to the strong fluorescence of the hosting mineral. No evidence of gases were detected.

9.3. Microthermometry

A summary of the FI micro thermometric data is reported in Table 4 and histograms of salinity and T_h are illustrated in Figure 14. All the FI types homogenized to L. The eutectic temperatures (T_e) for the type-A1 FI range -30 to -22.5 °C (mean of -25.3 °C), which are higher than eutectic temperature for the H_2O-NaCl system (Bodnar, 1993). The minimum recorded *Te* could be considered as the ternary eutectic point temperature (-23 °C) of the H_2O-NaCl-KCl system (Hall et al., 1988). Since minor amounts of CO_3^{2-} was detected by Raman spectroscopy studies inside type-A1 FI, the higher recorded T_e values could be explained by the presence of variable amounts of other components, such as Na_2CO_3 (K_2CO_3?) in addition to NaCl and KCl. The final ice-melting ($T_{m\text{-}ice}$) temperatures range from -3.7 to -0.6 °C (n = 44), which corresponds to salinities between 6.85 and 1 wt.% NaCl eq. (with a mode of 3.85 wt.% NaCl eq). Type-A1 shows the highest homogenisation temperature (T_h) estimates, ranging 298-365 °C and a well-defined mode at 340 °C (mean value of 333 °C). These values are similar to those obtained by Nabatian et al. (2017b) on the same FI type.

The T_e for the type-A2 FI range -31.5 to -23°C, with a mode at -23 °C, compatible with the ternary eutectic point temperature of the H_2O-NaCl-KCl system (Hall et al., 1988). The higher recorded values suggest the presence of other components as for type-A1. The $T_{m\text{-}ice}$ ranges from -3.7 to -0.1 °C (n = 195), which correspond to salinities between 6.0 and 0.18 wt.% NaCl eq., with a mean of 2.6 wt.% NaCl eq.. The T_h values distribute almost homogeneously in a wide range from 170 to 352 °C, with a mean at 272°C.

Due to the small size of type-A3 FI, the T_e were measured only in two cases, which provided -22 and -21 °C, respectively. The obtained values are close to the eutectic point temperature of H_2O-NaCl system. The $T_{m\text{-}ice}$ ranges from -2.6 to -1 °C (n = 52), which correspond to salinities between 4.3 and 1.7 wt.% NaCl eq., with a mean of 1.8 wt.% NaCl

eq. The T_h values range 232-365 °C, but the data are skewed to higher temperatures, with a mode at 310 °C.

The T_e for the type-A4 FI range -33 and -24 °C, with a mean of -27 °C. Since these FI are hosted in carbonate minerals, these T_e values can be attributed to the presence of CO_3^{2-} and/or ions such as Ca^{2+}, Mg^{2+}, Fe^{2+} in addition to H_2O+NaCl in the fluid. The $T_{m\text{-}ice}$ ranges from -1.2 to -0.1 (n = 91), which correspond to salinities between 2.1 and 0.2 wt.% NaCl eq., with a mean of 0.6 wt.% NaCl eq. The T_h values are distributed in a very wide range, from 145 to 300 °C, with a well-defined mode at 225 °C.

The salinity estimates for type-B FI were calculated only in four FI from the melting temperature of halite in the liquid phase upon heating. Halite crystals disappeared prior to the bubble in all FI. The calculated salinity estimates range from 30.5 to 32 wt.% NaCl eq. The average T_h spreads between 203 and 320 °C.

10. U-Pb zircon dating of magmatic rocks

The zircon U-Pb geochronological study was carried out on zircon separates as obtained both from the mineralised (sample MN03) and barren magmatic rocks (samples MN01, MN19 and MN31; Fig. 3 and Table 1). Few zircon grains were recovered from the andesitoid/basaltoid rocks (MN03 and MN31), whilst the acidic rocks (MN01 and MN19) provided a large number of grains. Zircons were first investigated through cathodoluminescence (CL), and back scattered electron (BSE) imaging techniques and then analysed in situ LA-ICP-MS system at the university of Nagoya, Japan (see the Appendix for the methodology and). Analytical results are summarized in Table 5.

MN03

Zircons are generally euhedral to subhedral. Zircon grains show short to long prismatic habits (usually >100 μm up to 500 μm), with length/width ratios 2:1 and up to 6:1. Most of the grains appear as nearly homogeneous in BSE images with rare brighter cores. Most of them possess a few continuous longitudinal fractures and apatite and feldspar inclusions are common. The CL images show oscillatory to sector growth zoning (Fig. 15a). The Th/U values are in the range 0.38-6.3 (n = 21; Table 5), compatible with an igneous origin (e.g., Rubatto, 2002; Kirkland et al., 2015). Despite discordance of some of the spot results due to Pb loss, the majority of the data define a nearly concordant cluster at about 33 Ma. In a Tera-Wasserburg Concordia diagram, an intercept age of 32.8 ± 1.1 Ma is obtained (2σ; MSWD = 3.5, n= 13) (Fig. 15b).

MN31

Most of the zircon grains are of small size (50 to 150 μm) and can be classified as type-1 subhedral to anhedral and type-2 euhedral crystals. Type-1 shows complex growth zoning with marginal resorption. Type-2 show oscillatory growth zoning (Fig. 15c). The Th/U values range between 0.3 and 2.57, attesting a magmatic origin. Age analyses of type-1 zircons reveals a large spread in apparent $^{206}Pb/^{238}U$ ages from 41.1 ± 1.6 to 2611 ± 70 Ma (Table 5). Type-2 zircons yielded the youngest apparent $^{206}Pb/^{238}U$ ages at ca. 30 Ma, with a Concordia age of 30.4 ± 1.2 Ma (2σ; MSWD = 0.12, n= 2) (Fig. 15d).

MN01

Zircon grains are generally euhedral to subhedral and show short to medium prismatic habits (usually >100 μm up to 250 μm), with length/width ratios of around 2:1. Most of the grains host abundant inclusions of Ap, Fsp, and Qz. The grains show heterogeneous zoning in BSE images with oscillatory and sector growth zoning in CL images. Xenocrystic cores are rarely preserved, and the cores are overgrown by oscillatory and sector zoned rims (Fig. 15e). Th/U values are systematically above 0.4. The majority of the apparent zircon $^{206}Pb/^{238}U$ ages from the growth zoning domains cluster at about 29 Ma, with a few grains providing early Cambrian (ca. 529 Ma) to the Upper Triassic (ca. 220 Ma) ages. A Concordia age of 28.9 ± 0.4 Ma (2σ, MSWD = 1.2; n=15) is obtained from the Oligocene zircon population (Fig. 15f).

MN19

Zircon grains are generally euhedral to subhedral and show short to long prismatic habits (usually >100 μm up to 300 μm), with length/width ration of 2:1 to 3:1. Most of the grains are heterogeneous and inclusion bearing in BSE images and some of them contain xenocrystic cores. In CL images, most of the grains show oscillatory and sector zoning in rim domains (Fig. 15g). The measured Th/U values are higher than 0.4. Most of the spots performed on the growth domains provided concordant ages, with a Concordia age of 28.3 ± 0.4 Ma (2σ, MSWD = 0.68; n=21) (Fig. 15h).

11. Molybdenite Re-Os geochronology

Two molybdenite-bearing samples were collected from V2b high-grade Mol veins (stage-2b mineralisation) from the core of the potassic alteration zone (Fig. 3 and Table 6) for Re-Os Mol geochronology (see Appendix). The two samples possess similar Re abundances (~19.3 and 22.1 ppm), and as they yield very similar Re-Os dates (below) also contain similar ^{187}Os

abundances (~12.2 and 13.9 ppb). The two samples yielded similar Re-Os dates of 28.3 ± 0.2 and 28.7 ± 0.2 Ma (Table 6). These ages are in excellent agreement with those previously presented for the SKMD (ca. 29 – 28 Ma) by Simmonds et al. (2019), but are in contrast with much older reported Re-Os Mol dates (ca. 42 Ma) by Nabatian et al. (2017b). The Re-Os Mol dating results of this study and those of Simmonds et al. (2019) also overlap with the U-Pb zircon ages (ca. 29-28 Ma) of the acidic magmatic bodies (samples MN01 and MN19) that intrude the main alteration zone (Fig. 3).

12. Rb -Sr geochronology of the alteration zone(s)

Several samples were selected for Rb-Sr geochronology in order to constrain the age of the fluid-driven alteration processes within the SKMD. Only sample MN02 (rock matrix) coming from the inner potassic-sodic alteration zone provided reliable results (see Table 7, Fig. 16). In other samples either Rb/Sr values of minerals like sericite or Kfs were too low to facilitate derivation of useful age information, or samples were affected by supergene alteration. Results for these samples will be reported elsewhere.

For sample MN02, the mineral assemblage in the matrix consists of the early-stage alteration products made of Kfs + Bt + Ap with minor amounts of Mol and Qz. Lately formed Ms (sericite) is also documented. We analyzed Bt, two grain size fractions of Kfs, Ap, and two grain size fractions of sericite. The age obtained for the primary assemblage Bt+ 2 Kfs+Ap is 33.3 ± 0.9 Ma with a MSWD (mean square weighted deviation) of 0.16, documenting that this sub-assemblage was in perfect Sr-isotopic equilibrium at that time. The late-stage Ms was formed by fluid-rock interaction and most probably grew at the expense of primary Kfs. Linear regression of the Rb-Sr data for 2 Kfs + Ap +2 Ms results in an age of 28.5 ± 1.8 Ma (MSWD = 6.3). It appears that there is slight Sr-isotopic disequilibrium between the two different grain size fractions of sericite, which slightly deteriorates the precision of the age but does not affect its accuracy.

13. Discussion

The zircon U-Pb geochronology from the ore-related intrusive bodies points to a multistage magma emplacement in the study area that, based on the petrographic characteristics, can be grouped in two main episodes of magmatism, at 33-30 Ma (basic to intermediate in composition) and at ca. 29-28 Ma (acidic in composition), respectively. The

early episode of magmatism is compatible with the early Oligocene U-Pb zircon ages reported in Simmonds et al. (2019) on the same mineralised body.

These magmatic episodes are associated with chronologically distinct alteration/mineralisation types, as discriminated by the Rb-Sr multimineral and Re-Os Mol geochronology. In particular, the Rb-Sr geochronology documented an early Bt-Kfs-Ap assemblage at ca. 33 Ma and a subsequent Ms-bearing one at ca. 28 Ma, thus coeval with the early basic and late acidic magmatic episodes, respectively. We can thus infer the two-stage Mo mineralisation as defined by the textures and mineralogical assemblages in the SKMD (Fig. 10) was polyphase and the consequence of : (i) an early low-grade, disseminated-type mineralisation (stage-1) at ca. 33 Ma, associated with the pervasive potassic-sodic alteration during basic to intermediate magmatism; and (ii) a subsequent, high-grade focused stockwork mineralisation (stage-2) at ca. 29-28 Ma, associated with Qz-Fsp veining and subsequent Cb precipitation during acidic magmatism. This evidence suggests a long-lived (at least 4-5 Ma) period of magma production, differentiation and emplacement to sustain the Mo mineralisation episode(s) in the study area.

To form an economic porphyry Mo mineralisation, a significant and multiple magma supply and differentiation within a large magma chamber, is needed to endow reasonable quantities of Mo (e.g., Candela and Holland, 1986; Candela, 1992; Robb, 2004; Audétat, 2010; Zhang et al., 2018). The lack of Cu mineralisation in the SKMD, which is at odds with the all known porphyry systems along the Urumieh-Dokhtar magmatic zone (supplementary material #1), also supports a scenario of a long-lasting magma crystallisation and differentiation in the chamber(s), which efficiently led to Cu extraction from the melt to the crystallizing marginal zones into sulfide minerals (e.g., Candela and Holland, 1986; Blevin and Chappell, 1992; Candela, 1992; Klemm et al., 2008; Audétat, 2010). The residual melt magma from such a chamber is then expected to show depletion in Cu and relative enrichment in Mo. With progressive crystallization, a more acidic, fluid-rich magma is produced which would be more fertile with respect to Mo (e.g., Candela and Holland, 1986; Candela, 1992; Robb, 2004; Audétat, 2010; Seo et al., 2012).

The longevity of magma chamber(s) could be simply related to the amount of primitive magma nesting deep in the crust (Hawkesworth et al., 2000), the water content of the magma that prevented magma to rise to the same crustal levels unlike its drier equivalent (Robb, 2004), or input of numerous batches of magmas from the deep crustal melt reservoir (Glazner et al., 2004).

13.1. Source of the Mo-bearing magma

Apparently, there is a good correlation between Re concentration values in Mol and source of the parental magma. In particular, high (hundred ppm) and low (few ppm) Re contents have been reported in many studies and were referred to as mantle- or to crust-derived magmas, respectively (e.g., Stein et al., 2001; Berzina et al., 2005; Mao et al., 2006; Wu et al., 2017). However temperature of Mol deposition (Ishihara, 1988), the alteration type within the same deposit (Newberry, 1979), and the availability of molybdenite could affect the amount of Re concentrations. Furthermore, based on Nd and Sr isotopic studies, Farmer and DePaolo (1984) proposed that the Cu source is in the mantle and the Mo source in preexisting crust. Many studies have also documented that the most fertile sources for syn- and post-collisional porphyry deposits is a subduction-modified lithosphere (Pettke et al., 2010; Richards, 2015).

Molybdenite samples from Tertiary porphyry deposits in Iran show a general positive correlation between higher Re concentration and younger ages (Taghipour et al., 2008; Mirnejad et al., 2013; Aghazadeh et al., 2015; Simmonds and Moazzen, 2015; Nabatian et al., 2017a; 2017b). It was therefore proposed that the Neogene magmas along UDMZ were less contaminated by crustal materials (Nabatian et al., 2017b).

The Re contents in the molybdenite samples analysed in this study (19-22 ppm), together with those presented in Simmonds et al. (2019), ranging 10-41 ppm, are remarkably lower than all other porphyry Cu-Mo (Au) systems along the Urumieh-Dokhtar magmatic zone, which are typically above 100 ppm (e.g., Aghazadeh et al., 2015). Significant in this regard is the presence of inherited zircons within both the early (dated at 33-30 Ma) mafic to intermediate and late (dated at 29-28 Ma) acidic magmatic rocks cropping out in the mineralised area (Table 5). These inherited zircons also show resorbed and heterogeneous textures (Fig. 15d), compatible with renewed melting and corrosion (Corfu et al., 2003). In this regard, various papers have outlined the dominant role of juvenile lower crust in metal endowment in porphyry Mo (e.g., Berzina et al., 2015; Liu et al., 2015; Zeng et al., 2015; Zhang et al., 2018) and Cu deposits along southern UDMZ (Asadi et al., 2014). We therefore suggest that the molybdenite Re contents from the SKMD most likely derive from a crustally-contaminated mantle sourced magma. This is in line with the calculated initial isotopic Sr composition of ~0.70497 as derived from sample MN02 (Fig. 16) that is indicative of a mantle-derived magma with minor crustal contaminations (Zindler and Hart, 1986).

598

599 ***13.2. Structural control on fluid flow and mineralisation***

600 The Mo mineralisation SKMD is structurally controlled as documented by the
601 development of a network of polyphase veining. Overall, the vein arrays are non-systematic,
602 as indicated by a nearly radial pattern of jointing within the main alteration zones (Fig. 6b-c),
603 and the Mol abundance in veins (V2a and V2b) decrease significantly when moving from the
604 inner potassic-sodic alteration zone focused on the main intrusive body to the outer Eocene
605 volcanic host rocks (Fig. 3). Similarly, the intensity of the phyllic alteration changes from
606 intense to low when crossing the contact between the mineralised porphyry and the volcanic
607 host rocks. This evidence suggests that the original intrusive contacts constituted a major
608 structural/rheological boundary that likely acted as a permeability barrier for the fluids
609 exsolved from the crystallizing intrusion (e.g., Oliver and Bons, 2001; Rossetti et al., 2007).
610 Significantly, within the ore body the vein array is more systematic in the transition
611 from V2a to V2b mineralisation stages and in the marginal propylitic alteration zone (Fig. 6).
612 In particular, the occurrence of a nearly orthogonal vein set in the potassic-sodic and
613 propylitic alteration zones points to a geological setting dominated by a horizontal biaxial
614 tensile stress field in an extensional regime (vertical maximum principal stress σ_1) and
615 characterized by reversal of the intermediate (σ_2) and minimum (σ_3) principal stress (Rives et
616 al., 1994; Caputo, 1995) between the NS and E-W paleo-directions. Since the main vein
617 strike distribution cluster around the E-W strike (Fig. 6), the regional σ_3 paleo-direction
618 during the main stage of Mol mineralisation is inferred to trend NS. Therefore, a transition
619 from a nearly isotropic stress field to a differential stress regime dominated by a N-S directed
620 σ_3 direction is envisaged. This also suggests a different style of structural control on ore
621 mineralisation, likely controlled by the fluid pressure changes in the mineralising
622 environment: from early hydrofracturing and stockwork vein arrays under supralithostatic
623 fluid pressures conditions to late planar vein arrays formation under sub-lithostatic
624 conditions.

625 ***13.3. Fluid evolution and the mineralising environment***

626 No information is provided in this study regarding the fluid(s) geochemistry
627 responsible for the main potassic-sodic alteration and associated disseminated stage-1 Mol
628 precipitation. The main products of this stage fluid(s) (as disseminated and micro-vein types)
629 are Kfs+Ab+Bt+Mt+Po, which is the common high-temperature mineral assemblage in the
630 early stages (orthomagmatic) of porphyry systems (e.g., Shinohara et al., 1995; Seedorff et

al., 2005; Sinclair, 2007; Sillitoe, 2010), including Mo deposits (e.g., Questa, Bloom, 1981; and Hudson Bay Mountain, Klemm et al., 2008). This is in line with the compositional layering in the porphyry stock (Fig. 5a), which suggests magma degassing close to the carapace of the rising intrusive body (Sinclair, 2007; Lawley et al., 2010). A magmatic origin for this stage-1 fluids is thus tentatively proposed indicated by the ubiquitous unidirectional solidification textures observed in potassic-sodic alteration zone as it proposed at MAX (Lawley et al., 2010) and Henderson (Shannon et al., 1982) porphyry Mo for the early stage fluids (Lawley et al., 2010). The transition from an oxidising to a reducing mineralising environment is attested by the sequential formation of magnetite, to ilmenite and pyrrhotite (Fig. 10), which can be associated to the Mol-I disseminated precipitation.

The early ore-bearing fluids (type-A1 and A2 FI) in V2a quartz veins (Mol-II mineralisation) show T_e values (-22.5°C to -33°C) consistent with a H_2O-NaCl-KCl system (Hall et al., 1988), with variable amounts of other cations such as Ca^{2+}, Mg^{2+}. Quartz geochemistry has demonstrated a hydrothermal (magmatic) origin for the mineralising fluid(s) (Fig. 11). The presence of CO_2 in the type-A1 FI may thus indicate an originally low-salinity and low CO_2-bearing magma-derived fluid(s). The association of low saline fluids, usually containing low amounts of CO_2, is common in porphyry Mo deposits, in particular within arc-related Mo deposits, such as Endako (Selby et al., 2000), Thompson Creek (e.g., Thompson Creek, Hall et al., 1984; Cannivan Gulch, Darling, 1994; Geumeum, Kim et al., 2016), and, apparently, it has no effect on the size or the ore-grade of the deposit (Taylor et al., 2012). Cline and Bodnar (1991, 1994) have demonstrated that when magma crystallization progresses, the released fluid(s) will have less than 10% chlorine concentration. Since we do not have firm evidence of fluid boiling from the FI assemblage, the rare type-B, high saline (up to 32 wt.% NaCl eq.) fluids in FIs can hence be interpreted as magma-sourced saline brines, segregated in the early stages of magma crystallization (Cline and Bodnar, 1991; 1994). Alternatively, fluid boiling could have occurred at deeper levels, predating the Mol mineralization. The vaporization of CO_2 during boiling could have increased the pH, leading to precipitation of Cu from the fluids (Drummond and Ohmoto, 1985), whereas Mo remained dissolved in the residual fluids with lower salinity and CO_2 content as hydroxyl (H_2MoO_4) and alkali molybdate complexes (Ulrich and Mavrogenes, 2008). In addition, boiling and the associated early metal deposition could have consumed the sulphur, increasing further the solubility of Mo in the residual fluids (Xiaoyun, 1989; Ulrich and Mavrogenes, 2008).

Fluids from the phyllic alteration zone (type-A3 FI) show no evidence of CO_2 but similar T_h (240-350 °C) and salinity (1.7-4.3 wt.% NaCl eq.). This is comparable with the Endako porphyry Mo deposit, where the fluid chemistry associated with K-feldspar and sericite alteration assemblages show no distinct differences (Selby et al., 2000). A significant contribution of meteoric fluids is inferred due to the absence of CO_2 and the observed lower T_h and salinities. The paragenetic occurrence of Ser (Ms) with Mol+Cb mineralisation (Mol-III mineralisation) highlights the dominant role of neutralisation and cooling of acidic fluids (Hemley and Hunt, 1992; Giggenbach, 1997) caused by percolating meteoric fluids and mixing, which also caused the sulphide precipitation. Moreover, the coincidence of high-grade Mo precipitation with very low salinity type-A4 FI could be explained by the importance of hydroxyl complex (H_2MoO_4, Ulrich and Mavrogenes, 2008) for molybdenum transportation (Candela and Holland, 1986) in temperatures below 300 °C (Xiaoyun, 1989). Since the Mo solubility decreases with increasing salinity (Keppler and Wyllie, 1991), Mo precipitation should have been facilitated by continuous fluid exsolution and mixing, temperature/pressure fluctuations and/or pH changes (Audétat, 2010; Seo et al., 2012).

In order to better constrain the thermo-baric environment associated with Mo mineralisation, FI isochores (Fig. 17a) have been constructed using the BULK and ISOC softwares (Bakker, 2003). Isochores were chosen considering representative fluid inclusions for type-A1 (bulk density of 0.599 g/cc) and A-4 (bulk density of 0.826 g/cc) FI. Calculations were based on the equations of state of Zhang and Frantz (1987) for density and Bodnar (1993), Bodnar and Vityk (1994), and Knight and Bodnar (1989) for the bulk composition. The isochores are then combined with the T estimates as derived from the TitaniQ thermometry for pressure correction. For the type-A1, the area in P–T space defined by the intersections of isochores with T estimates is centered at 1.5 ± 0.5 kbar and 580° ± 75°C. Assuming lithostatic pressure conditions, this conforms to paleogeothermal gradient of ca. 100 °C/km and a depth of 7.4 km (based on a lithostatic pressure gradient of 27 MPa km^{-1}) for the early (V2a stage) mineralisation. This pressure/depth estimates for the mineralising environment is consistent with those reported in many porphyry Mo deposits (Selby et al., 2000; Taylor et al., 2012; Ni et al., 2015). This is also compatible with the marginal magmatic textures (compositional layering) preserved at the roof of the main mineralised body (Fig. 5a). Using the same geothermal gradient and assuming a progressive transition from lithostatic to hydrostatic pressure conditions, the intersection with the type-A4 isochore provides pressure estimates ranging from 0.25 (based on a hydrostatic pressure gradient of 10 MPa km^{-1}) to 0.75 kbar in a narrow temperature range of ca. 250 °C. These P-T estimates

698 constrain the high-grade Mo mineralisation during the V2b stage at shallower crustal levels
699 (ca. 3 km) during progressive exhumation of the mineralising system (Fig. 17a).
700 When the different FI types are plotted in a Th vs. salinity diagram, there is a
701 significant overlap in the populations of L-rich+V FI. Nonetheless, a general trend of
702 decreasing Th and salinities values from Type-A1, A2 and A3 (hosted by quartz) to type-A4
703 (hosted by paraspurite) FI can be observed (Fig. 17b). Three main groups of FI can be
704 discriminated in the Th vs. salinity diagram: (i) group-1, with the highest mean of Th, that
705 includes all the type-A1 and part of the type-A2 FI; (ii) group-2 that includes the type-A2 FI,
706 with a general trend to lower Th and salinity values; and (iii) group-3, formed by the type-A4
707 FI. Taking into consideration the fluid evolution processes typical of hydrothermal ore
708 deposits depicted in Wilkinson (2001), group-1 is consistent with isothermal mixing and
709 group-2 with meteoric fluid mixing/dilution, respectively. Group-3 is instead consistent with
710 cooling and pressurisation (Fig. 17b-c). This evidence suggests a mineralising system
711 recording the progressive evolution from a closed to an open fluid circulation system,
712 controlled by the progressive transition from a ductile to brittle environment, where rock
713 fracturing has enhanced permeability and meteoric fluids percolation and mixing.

714 ***13.4. A model for the Siah Kamar Mo mineralisation***

715 Collectively, our results from the SKMD confirm a Mo mineralisation scenario
716 compatible with an Endako-type porphyry Mo deposit (see also Nabatian et al., 2017b).
717 Nonetheless, our results also point to peculiar characteristics for the SKMD. The main
718 peculiarity of the SKMD is a prolonged history of magma production and emplacement (ca.
719 4-5 Ma). In fact, despite that multiple magma intrusion processes are common in the
720 evolution of porphyry systems, the time lapse from early- to late-stage mineralisation is
721 usually less than 1 m.y. (Sillitoe, 2010; Mercer et al., 2015). Therefore the SKMD can be
722 classified as an uncommon porphyry Mo mineralization, which operated in a time scale of at
723 least 4-5 Ma. Such mineralisation time scales have been reported from giant and large
724 porphyry systems (e.g., Chuquicamata, Correa et al., 2016; and Halasu, Xue et al., 2016).
725 The concurrence of carbonatization and Mol mineralisation is also a peculiar
726 characteristic of the SKMD. Carbonate precipitation is uncommon in porphyry systems
727 (Taylor et al., 2012) and carbonate veins commonly, which occurred in the latest stages, are
728 either barren (e.g., Selby et al., 2000; Seedorff and Einaudi, 2004; Mao et al., 2011; Ni et al.,
729 2015) or with only minor Mo enrichment (e.g., Yang, 2007; Wang et al., 2017; Zhai et al.,
730 2017).

Therefore, any model for the formation of the Mo Siah Kamar mineralisation should take into consideration the following constraints: (i) the U-Pb zircon magmatic ages and the Rb-Sr ages of the alteration mineralogy support a two-stage mineralisation process: early (at ca. 33 Ma) low-grade disseminated mineralization (stage-1, Mol-I) during potassic-sodic alteration in a reducing environment and subsequent (at ca 28-29 Ma) high-grade stockwork Mo mineralisation (stage-II, Mol-II and Mol-III, as constrained by the Re-Os Mol geochronology) during phyllic alteration; (ii) the two-stage mineralisation is associated with multiphase intrusions and transition from basic to acidic magmatism, in a time lapse of ca. 4-5 Ma; (iii) the mineralising fluid(s) records transition from a magmatic/hydrothermal- to a meteoric-dominated system across a progressive ductile-to-brittle environment (temperature range from ~600 to 250 °C); and (iv) the dominant role of carbonate precipitation and neutralisation of acidic fluids in the Mo mineralisation (Mol+Ser+Cb assemblage) during fluid cooling.

Based on the synchronicity (in the time lapse 28-29 Ma) existing between the crystallisation of the acidic dyke and stock at the rims of the mineralised zone (Fig. 3), phyllic alteration and Mo-mineralisation, it is postulated that mineralising fluids were sourced from these acidic intrusives. Nonetheless, these acidic magmatic rocks are Mo-barren. We then propose a model of Mo mineralisation as primarily caused by the re-fertilisation (ore enhancement) induced by the renewed magma supply at 28-29 Ma. The exposed acidic intrusions are considered as the apophyses of a magmatic system likely supported by a voluminous magma chamber at depth, able to sustain highly perturbed geothermal conditions and renewed fluid supply within the early formed potassic-sodic alteration zone formed at ca. 33 Ma (Fig. 18). In such a scenario, the mode of fluid exsolution was controlled and modulated by the rheological evolution of the solidifying shell surrounding the cooling magma. At high-temperature conditions (T>600 °C), fluid-rock equilibrium was likely attained and fluids were entrapped in solidifying magma at depth (ca. 7 km). When temperature decreased and brittle deformation prevailed, more fluids were released into the system and interacted with the ground waters (e.g., Giggenbach, 1997). At this stage (T< 300°C), the CO_2 dissolved in the fluids became reactive and the release of CO_2 caused acidification of the fluids (Giggenbach and Soto, 1992; Kaszuba et al., 2005; Little and Jackson, 2010) and significant interaction with the country rocks, leading to mineral dissolution and metal leaching (Bandstra and Brantley, 2008; Liu et al., 2012; Kirsch et al., 2014; Lions et al., 2014) from the early-formed potassic-sodic alteration zone. The deposition zone is thus interpreted as zone of fluid mixing with meteoric ground water, when fluid

neutralization and temperature drop down leading to the Ms-Cb precipitation and metal (Mol) mineralisation in the system, focused by structurally-controlled pathways assisted by continuous fracturing of the intrusive carapace.

13.5. Correlation at regional scale

Similar Eocene-Oligocene high-K calc-alkaline to shoshonitic magmatism as reported from the SKMD (Khaleghi et al., 2013; Nabatian et al., 2017b) has been also reported in many studies along the UDMZ, AMZ, BAMZ, Lesser Caucasus, and the western Alborz (e.g., Aftabi and Atapour, 2000; Ahmadian et al., 2009; Aghazadeh et al., 2010; Sarjoughian et al., 2012; Kananian et al., 2014; Jamali and Mehrabi, 2015) (Fig. 1). Within this context, the SKMD shows the oldest reported ages among the porphyry deposits within the UDMZ (except the Kal-e-Kafi porphyry Cu-Mo deposit, with zircon U-Pb age of 52-50 Ma, Ahmadian et al., 2016), and only two porphyry Cu-Mo-Au deposits have been reported within the same time window including Bondar-e-Hanza (with Mol Re-Os age of 28.4 ± 0.5 Ma, Aghazadeh et al., 2015) and Reagan (with zircon U-Pb age of 29.3 ± 0.2 Ma, Hassanzadeh, 1993) (Fig. 1 and supplementary material #1).

By contrast, many porphyry Cu-Mo deposits with older (Eocene) and similar (Oligocene) ages have been reported in the AMZ (Haftcheshmeh Cu-Mo, Mol Re-Os age of 28.2-27.1 Ma, Aghazadeh et al., 2015) and Lesser Caucasian magmatic zones (Kadjaran Cu-Mo; 27.3–26.4 Ma, Rezeau et al., 2016). Nonetheless, apart from the SKMD, none of these porphyry systems shows Mo as the first commodity. In particular, whereas the Mo/Cu ratio within SKMD is about 1, the coeval porphyry Cu-Mo deposits of Kadjaran, Haftcheshmeh, and Kal-e Kafi show values of about 0.1, which are significantly higher than the Miocene ones (supplementary material #1). The Mo enrichment in the Eocene-Oligocene porphyry systems could be attributed to either to a relatively deeper emplacement level of the metal-bearing magma (Candela, 1986) or to the contribution and re-fertilisation of a preexisting Mo-enriched crustal source (Farmer and DePaolo, 1984; Wan et al., 2018).

14. Conclusions

The main results of this study can be summarised as follows:

(1) The SKMD developed during a long-lived magmatic and alteration history, spanning from ca. 33 Ma to 29-28 Ma, associated with a diachronous, low- and high-grade Mo mineralisation.

(2) Re-fertilisation of an early formed disseminated Mo ore by renewed magmatism and associated magma degassing and fluid exsolution is proposed as the scenario for ore enhancement and, consequently, for high-grade Mo mineralisation.
(3) Leaching of metals from the early formed disseminated ore bodies operated by acidic fluids exsolved from the cooling magmas is recognised as the cause of Mo-enrichment in the mineralising fluids.
(4) Mixing of magmatic and meteoric fluids during progressive embrittlement (and cooling) of the mineralising environment is considered as the key factor leading to the high-grade Mo ore formation, through progressive neutralisation of the acidic fluids via structurally-controlled carbonation and sericitisation.

Comparison at a regional scale indicates that parameters such as longevity of magma supply, progressive magma crystallization/differentiation and the presence of a possible pre-enriched crustal material should be considered for the Mo endowment in the UMDZ.

Acknowledgements

This research is part of the first Author PhD program at the Roma Tre University. The Grant to Department of Science, Roma Tre University (MIUR-Italy Dipartimenti di Eccellenza, ARTICOLO 1, COMMI 314 – 337 LEGGE 232/2016) is gratefully acknowledged. DS – Total Endowment Fund, CUG Dida Scholarship, Antonia Hofmann, Chros Ottley, Geoff Nowell. We are indebted to K. Yamamoto for support and providing access to the XRF, ICP-MS and LA-ICP-MS facilities at Nagoya University. We thank T. Theye for advice and for granting access to electron microprobe and LA-ICP-MS facilities at the Institut für Mineralogie und Kristallchemie at the University of Stuttgart. We also thank C. Romano for granting access to the Raman Spectroscopy facility at the Department of Science, Roma Tre University. We thank the Aria Kansar Samin Co for sharing their data on the Siah-Kamar Mo deposit and for granting access to the mineralisation area. This manuscript benefitted of constructive comments and advice from D. Lentz and an anonymous reviewer. We also thank the editorial handling by F. Pirajno.

827

828 **APPENDIX:**

829 **Analytical techniques**

830 **LA-ICP-MS quartz trace element geochemistry**

831 Based on petrographic observations (optical and BSE) and mineral chemistry on polished
832 thin-section samples, 16 representative quartz crystals were selected for in situ trace and
833 REEs element analyses, using laser ablation (LA, CETAC LSX-213 laser system) combined
834 with an inductively coupled plasma mass spectrometer (ICP-MS, AGILENT 7700) at Institut
835 für Mineralogie, Universität Stuttgart. The following laser ablation parameters were used:
836 spot diameter 50 µm, 60% laser power (100% = 4 mJ at a spot diameter of 150 µm), 10 Hz
837 laser pulse repetition rate, and a mixed helium and argon gas flow with 500 ml/min and 800
838 ml/min, respectively, serving as carrier of the ablated material.
839 The data acquisition was performed using the Agilent Mass Hunter software (version
840 B.01.01). Each analysis comprised the acquisition of the individual background ion
841 intensities (gas-blank) for roughly 23 s followed by the acquisition of the ion intensities on
842 laser irradiation of the sample spot for roughly 57 s.
843 The method involved monitoring of 18 isotopes (7Li, 9Be, 11B, 27Al, 28,29Si, 31P, 44Ca,
844 47,49Ti, 55Mn, 56,57Fe, 71Ga, 72,73Ge, 75As, 85Rb, 88Sr; this selection excludes isobaric
845 interferences of isotopes from other elements) using individual integration times of 10 ms.
846 Reference materials were DLH7 and DLH8 glasses from P&H Developments Ltd., and
847 NIST (National Institute of Standards and Technology, USA) 612 and 610 glasses. Certified,
848 recommended and proposed values for these reference materials are from Jochum et al.
849 (2011). The validity of the calibration, data evaluation, and reproducibility were checked
850 with the reference materials Diorite (DRN) and Zinnwaldite (ZW-C) from Service
851 d'Analyses des Roches et des Mineraux du CNRS. Lithium-borate glass disks of both were
852 prepared using 0.6 g of powder of these reference materials and 3.6 g of lithium borate. All
853 elemental concentrations were calculated relative to the silicon elemental concentration as
854 internal standard which was determined from the results of the 29Si isotope. The absolute
855 silicon concentration was previously measured with the EMP. The same spot target was
856 applied for both EMP and LA-ICP-MS. Precision is estimated better than 5%. The software
857 used for calibration and data evaluation was developed by J. Opitz (Massonne et al., 2013;
858 Baggio et al., 2018).
859

Fluid inclusion microthermometry

Samples representative of the different mineralised quartz-carbonate vein sets were prepared as 150- μm-thick doubly polished wafers and petrography studies were carried out with a polarizing microscope to define the types of fluid inclusions, the populations and their genetic relationships. Microthermometric measurements were made utilizing a Linkam THMSG600 freezing– heating stage at the Istituto di Geologia Ambientale e Geoingegneria of CNR at the University of Roma ‘‘La Sapienza’’. The systems were calibrated using pure natural CO2 inclusions for low temperatures and synthetic pure water fluid inclusions for high temperatures, respectively. Reproducibility of the triple point of CO_2 at –56.6 °C and pure H_2O critical point at 374 °C were ± 0.3°C and ± 0.5 °C respectively. Low temperature (Te, Tm) data were determined with a 1–5 °C/min rate, whereas high temperature (Th, Tms) data with a heating rate of 5–20°C/min, respectively. Bulk composition and Isochores for various FI types were calculated by BULK and ISOC softwares provided by (Bakker, 2003).

Raman spectroscopy

A HORIBA LabRAM HR Raman spectrometer at the Dipartimento di Scienze, Università degli Studi di Roma Tre, calibrated using a silicon standard, was employed to acquire the Raman spectra. The micro-Raman spectrometer is equipped with a green argon ion laser (532 nm), focused through a 50× and 100× objectives. Optical filters were employed in order to achieve ~2.5 mW at the surface of the glassy interface. The Raman systems were set with 600 T and 1200 T gratings, exposure time 20 s (3 times), confocal hole of 200–500 μm, and slit of 200 μm, and the spatial resolution of the sample surface is ~1 μm (theoretical spatial resolution = 0.61 λ/NA where λ is the wavelength of the laser (532 nm), and NA is the numerical aperture of the microscope objective being used (0.9 for 100×). Raman spectra were acquired over the range from 90 to 2000 cm^{-1}. Reference values from Frezzotti et al. (2012) for common gases inside fluid inclusions and some minerals were used to interpret the obtained spectra. Furthermore, the CrystalSleuth software (http://rruff.info/) was employed to define the accessory minerals.

Zircon U-Pb Geochronology

The zircon U-Pb geochronology study was carried out at the Department of Earth and Environmental Sciences of Nagoya University. Four samples were selected for zircon grains separation. More than 10 kg for each sample were collected and crushed. Only few zircon grains (ca. 30) were found. Some of them were useless due to the small grain size (< 30 □m) or to the strongly fractured crystal structure. Cathodoluminescence (CL) and Back Scatter

(BSE) imaging was used first to gather information on the grain texture and internal growth and/or alteration zoning. Zircon grains with intense fracturing and inclusions were avoided. The zircon grains were analyzed by LA-ICP-MS (Agilent 7700XICPMS machine connected with NWR213 (Electro Scientific Industries) laser ablation system (Kouchi et al., 2015). A standard glass (NIST SRM 610) and two zircon standards, named 91500 (1059 Ma, Wiedenbeck et al., 1995) and OD-3 (33.1 Ma, Iwano et al., 2013) were used. Blanks, the zircon standards, and the standard glass were measured at the beginning and ending of each measurement cycle. Eight points were measured in each cycle. The ISOPLOT V4.15 software (Ludwig, 2011) was utilized to calculate the Concordia, statistics and to prepare the age plots. Correction for the common Pb was performed using ^{204}Pb intensity (Cox and Wilton, 2006). Most of the results with high common Pb (values more than 20 %) were excluded from calculations.

Molybdenite Re-Os geochronology

Molybdenite grains were isolated from samples and then gently were milled, washed and dried (Selby and Creaser, 2004). Impurities were separated under microscope and about 100 mg of pure molybdenite was prepared for each sample with the analytical protocol following that of (Selby and Creaser, 2004). The Re-Os molybdenite analysis were performed in the Laboratory for Sulfide and Source Rock Geochronology and Geochemistry and the Arthur Holmes Laboratory in the Durham Geochemistry Centre at Durham University (UK). In brief, molybdenite samples were dissolved and equilibrated with a known amount of ^{185}Re and isotopically normal Os in inverse aqua regia (2:1 16 N HNO3 and 12 N HCl, 3 mL) at 240 °C for 24 h in a Carius-tube. Rhenium and Os were isolated and purified by solvent extraction, microdistillation, and anion exchange chromatography, and analyzed by negative thermal ionization mass spectrometry on a ThermoScientific TRITON mass spectrometer using Faraday collectors. Total procedural blanks for Re and Os 2.5 pg and 0.1 pg, respectively, with an Os blank composition of 0.21 0.02 (n 6), which are insignificant to the Re and Os levels in the analysed samples. Rhenium and Os concentrations, and Re-Os molybdenite date uncertainties are presented at the 2σ level, which includes the uncertainties in Re and Os mass spectrometer measurement, spike and standard Re and Os isotopic compositions, and calibration uncertainties. Because a mixed tracer solution is used, uncertainties in weights of sample and tracer solution do not affect the calculated age, and are not considered. However, sample and tracer solution weight uncertainties are considered in

925 determining the uncertainty in the Re and ^{187}Os concentrations. Uncertainty in the ^{187}Re
926 decay constant (0.35%, Smoliar et al., 1996)) is also considered.
927
928 **Rb-Sr multimineral geochronology**
929 To determine the ages of mineral assemblage crystallization, we employed the Rb-Sr
930 internal mineral isochron approach. Age information mainly is based on the high-Rb/Sr
931 phases muscovite/sericite, and biotite. Mineral separates were prepared following Glodny et
932 al. (2008). Crushing was performed by hand using pestle and mortar combined with repeated
933 sieving, to preserve the original grain sizes of minerals. Rb–Sr isotopic data were acquired at
934 GFZ Potsdam using a Thermo Scientific TRITON thermal ionization mass spectrometer. Sr
935 isotopic compositions were measured in dynamic multi-collection mode. Rb isotope dilution
936 analysis was done in static multi-collection mode. The value obtained for $^{87}Sr/^{86}Sr$ of the
937 NIST SRM 987 reference material was 0.710255 ± 0.000024 (2σ, n = 23). For age
938 calculation, uncertainties of ± 0.005% for $^{87}Sr/^{86}Sr$ and of ± 1.5% for $^{87}Rb/^{86}Sr$ ratios were
939 assigned to the results. Uncertainties of isotope and age data are quoted at 2σ. The program
940 ISOPLOT/EX 4.15 (Ludwig, 2011) was used for calculating regression lines. Decay
941 constants are those recommended by Villa et al. (2015).
942

References

Aftabi, A., Atapour, H., 2000. Regional aspects of shoshonitic volcanism in Iran. Episodes 23, 119-125.

Aghanabati, A., 2004. Geology of Iran, GSI Publication, Tehran.

Aghazadeh, M., Castro, A., Omran, N.R., Emami, M.H., Moinvaziri, H., Badrzadeh, Z., 2010. The gabbro (shoshonitic)–monzonite–granodiorite association of Khankandi pluton, Alborz Mountains, NW Iran. Journal of Asian Earth Sciences 38, 199-219.

Aghazadeh, M., Hou, Z., Badrzadeh, Z., Zhou, L., 2015. Temporal–spatial distribution and tectonic setting of porphyry copper deposits in Iran: Constraints from zircon U–Pb and molybdenite Re–Os geochronology. Ore Geology Reviews 70, 385-406.

Ahmadian, J., Haschke, M., McDonald, I., Regelous, M., RezaGhorbani, M., Emami, M.H., Murata, M., 2009. High magmatic flux during Alpine-Himalayan collision: Constraints from the Kal-e-Kafi complex, central Iran. Geological Society of America Bulletin 121, 857-868.

Ahmadian, J., Sarjoughian, F., Lentz, D., Esna-Ashari, A., Murata, M., Ozawa, H., 2016. Eocene K-rich adakitic rocks in the Central Iran: implications for evaluating its Cu–Au–Mo metallogenic potential. Ore Geology Reviews 72, 323-342.

Amidi, M., Alavi Tehrani, M., Lotfi, P., Haghipour, A., Sabzehei, M., Behroozi, A., Lescuyer, J., Riou, R., 1987. Geological map of Mianeh. Geological Survey of Iran, Tehran.

Aria Kansar Samin Co., u.r., 2013. Report on exploratory operations of Siah-Kamar molybdenum occurrence.

Asadi, S., Moore, F., Zarasvandi, A., 2014. Discriminating productive and barren porphyry copper deposits in the southeastern part of the central Iranian volcano-plutonic belt, Kerman region, Iran: a review. Earth-Science Reviews 138, 25-46.

Audétat, A., 2010. Source and evolution of molybdenum in the porphyry Mo (–Nb) deposit at Cave Peak, Texas. Journal of Petrology 51, 1739-1760.

Audetat, A., Pettke, T., Heinrich, C., Bodnar, R., 2008. The composition of magmatic-hydrothermal fluids in barren and mineralized intrusions: ecoNomic geology, v. 103.

Ayati, F., Yavuz, F., Asadi, H.H., Richards, J.P., Jourdan, F., 2013. Petrology and geochemistry of calc-alkaline volcanic and subvolcanic rocks, Dalli porphyry copper–gold deposit, Markazi Province, Iran. International Geology Review 55, 158-184.

Ayres, L., Averill, S., Wolfe, W., 1982. An Archean molybdenite occurrence of possible porphyry type at Setting Net Lake, northwestern Ontario, Canada. Economic Geology 77, 1105-1119.

Babazadeh, S., Ghorbani, M.R., Bröcker, M., D'Antonio, M., Cottle, J., Gebbing, T., Carmine Mazzeo, F., Ahmadi, P., 2017. Late Oligocene–Miocene mantle upwelling and interaction inferred from mantle signatures in gabbroic to granitic rocks from the Urumieh–Dokhtar arc, south Ardestan, Iran. International Geology Review 59, 1590-1608.

Baggio, S.B., Hartmann, L.A., Lazarov, M., Massonne, H.-J., Opitz, J., Theye, T., Viefhaus, T., 2018. Origin of native copper in the Paraná volcanic province, Brazil,

986 integrating Cu stable isotopes in a multi-analytical approach. Mineralium Deposita 53,
987 417-434.

988 Bakker, R.J., 2003. Package FLUIDS 1. Computer programs for analysis of fluid
989 inclusion data and for modelling bulk fluid properties. Chemical Geology 194, 3-23.

990 Ballato, P., Cifelli, F., Heidarzadeh, G., Ghassemi, M.R., Wickert, A.D., Hassanzadeh, J.,
991 Dupont-Nivet, G., Balling, P., Sudo, M., Zeilinger, G., Schmitt, A.K., Mattei, M.,
992 Strecker, M.R., 2017a. Tectono-sedimentary evolution of the northern Iranian Plateau:
993 insights from middle-late Miocene foreland-basin deposits. Basin Research 29, 417-446.

994 Ballato, P., Cifelli, F., Heidarzadeh, G., Ghassemi, M.R., Wickert, A.D., Hassanzadeh, J.,
995 Dupont‐Nivet, G., Balling, P., Sudo, M., Zeilinger, G., 2017b. Tectono‐sedimentary
996 evolution of the northern Iranian Plateau: insights from middle–late Miocene
997 foreland‐basin deposits. Basin Research 29, 417-446.

998 Bandstra, J.Z., Brantley, S.L., 2008. Surface evolution of dissolving minerals
999 investigated with a kinetic Ising model. Geochimica et Cosmochimica Acta 72, 2587-
1000 2600.

1001 Berberian, M., King, G., 1981. Towards a paleogeography and tectonic evolution of Iran.
1002 Canadian Journal of Earth Sciences 18, 210-265.

1003 Berzina, A., Berzina, A., Gimon, V., Bayanova, T., Kiseleva, V.Y., Krymskii, R.S.,
1004 Lepekhina, E., Palesskii, S., 2015. The Zhireken porphyry Mo ore-magmatic system
1005 (eastern Transbaikalia): U–Pb age, sources, and geodynamic setting. Russian Geology
1006 and Geophysics 56, 446-465.

1007 Berzina, A.N., Sotnikov, V.I., Economou-Eliopoulos, M., Eliopoulos, D.G., 2005.
1008 Distribution of rhenium in molybdenite from porphyry Cu–Mo and Mo–Cu deposits of
1009 Russia (Siberia) and Mongolia. Ore Geology Reviews 26, 91-113.

1010 Blevin, P.L., Chappell, B.W., 1992. The role of magma sources, oxidation states and
1011 fractionation in determining the granite metallogeny of eastern Australia. Earth and
1012 Environmental Science Transactions of The Royal Society of Edinburgh 83, 305-316.

1013 Bloom, M.S., 1981. Chemistry of inclusion fluids; stockwork molybdenum deposits from
1014 Questa, New Mexico, Hudson Bay Mountain and Endako, British Columbia. Economic
1015 Geology 76, 1906-1920.

1016 Bodnar, R., 1993. Revised equation and table for determining the freezing point
1017 depression of H2O-NaCl solutions. Geochimica et Cosmochimica Acta 57, 683-684.

1018 Bodnar, R., Vityk, R., 1994. Interpretation of microthermometric data for H_2O-NaCl
1019 fluid inclusions. Fluid inclusions in minerals: Methods and applications. . Short course of
1020 the working group, Inclusions in Minerals, 117-130.

1021 Candela, P.A., 1992. Controls on ore metal ratios in granite-related ore systems: an
1022 experimental and computational approach. Earth and Environmental Science
1023 Transactions of The Royal Society of Edinburgh 83, 317-326.

1024 Candela, P.A., Holland, H.D., 1986. A mass transfer model for copper and molybdenum
1025 in magmatic hydrothermal systems; the origin of porphyry-type ore deposits. Economic
1026 Geology 81, 1-19.

1027 Caputo, R., 1995. Evolution of orthogonal sets of coeval extension joints. Terra Nova 7,
1028 479-490.

1029 Castro, A., Aghazadeh, M., Badrzadeh, Z., Chichorro, M., 2013. Late Eocene–Oligocene
1030 post-collisional monzonitic intrusions from the Alborz magmatic belt, NW Iran. An
1031 example of monzonite magma generation from a metasomatized mantle source. Lithos
1032 180-181, 109-127.

1033 Cathles, L.M., Erendi, A., Barrie, T., 1997. How long can a hydrothermal system be
1034 sustained by a single intrusive event? Economic Geology 92, 766-771.

1035 Chiaradia, M., Merino, D., Spikings, R., 2009. Rapid transition to long-lived deep crustal
1036 magmatic maturation and the formation of giant porphyry-related mineralization
1037 (Yanacocha, Peru). Earth and Planetary Science Letters 288, 505-515.

1038 Chiu, H.-Y., Chung, S.-L., Zarrinkoub, M.H., Mohammadi, S.S., Khatib, M.M., Iizuka,
1039 Y., 2013. Zircon U–Pb age constraints from Iran on the magmatic evolution related to
1040 Neotethyan subduction and Zagros orogeny. Lithos 162, 70-87.

1041 Cline, J.S., Bodnar, R.J., 1991. Can economic porphyry copper mineralization be
1042 generated by a typical calc‐alkaline melt? Journal of Geophysical Research: Solid Earth
1043 96, 8113-8126.

1044 Cline, J.S., Bodnar, R.J., 1994. Direct evolution of brine from a crystallizing silicic melt
1045 at the Questa, New Mexico, molybdenum deposit. Economic Geology 89, 1780-1802.

1046 Colville, A.A., Colville, P.A., 1977. Paraspurrite, a new polymorph of spurrite from Inyo
1047 County, California. American Mineralogist 62, 1003-1005.

1048 Corfu, F., Hanchar, J.M., Hoskin, P.W.O., Kinny, P., 2003. Atlas of Zircon Textures.
1049 Reviews in Mineralogy and Geochemistry 53, 469-500.

1050 Correa, K.J., Rabbia, O.M., Hernández, L.B., Selby, D., Astengo, M., 2016. The timing
1051 of magmatism and ore formation in the El Abra porphyry copper deposit, northern Chile:
1052 Implications for long-lived multiple-event magmatic-hydrothermal porphyry systems.
1053 Economic Geology 111, 1-28.

1054 Cox, R.A., Wilton, D.H., 2006. U–Pb dating of perovskite by LA-ICP-MS: an example
1055 from the Oka carbonatite, Quebec, Canada. Chemical Geology 235, 21-32.

1056 Darling, R.S., 1994. Fluid inclusion and phase equilibrium studies at the Cannivan Gulch
1057 molybdenum deposit, Montana, USA: Effect of CO_2 on molybdenite-powellite stability.
1058 Geochimica et Cosmochimica Acta 58, 749-760.

1059 Dennen, W., 1966. Stoichiometric substitution in natural quartz. Geochimica et
1060 Cosmochimica Acta 30, 1235-1241.

1061 Doebrich, J.L., Garside, L.J., Shawe, D.R., 1996. Characterization of mineral deposits in
1062 rocks of the Triassic to Jurassic magmatic arc of western Nevada and eastern California.
1063 Citeseer.

1064 Drummond, S., Ohmoto, H., 1985. Chemical evolution and mineral deposition in boiling
1065 hydrothermal systems. Economic Geology 80, 126-147.

1066 Duke, C.P., 2007. Pidgeon Molybdenum project: Toronto, Ontario, Wardrop Engineering
1067 Inc., NI 34–101 Compliant Report for MPH Ventures Corporation. 92.

1068 Farmer, G.L., DePaolo, D.J., 1984. Origin of Mesozoic and Tertiary granite in the
1069 western United States and implications for Pre-Mesozoic crustal structure: 2. Nd and Sr
1070 isotopic studies of unmineralized and Cu- and Mo-mineralized granite in the Precambrian
1071 Craton. Journal of Geophysical Research: Solid Earth 89, 10141-10160.

1072 Fazel, E.T., Mehrabi, B., Shabani, A.A.T., 2015. Kuh-e Dom Fe–Cu–Au prospect,
1073 Anarak metallogenic complex, Central Iran: a geological, mineralogical and fluid
1074 inclusion study. Mineralogy and Petrology 109, 115-141.

1075 Frezzotti, M.L., Tecce, F., Casagli, A., 2012. Raman spectroscopy for fluid inclusion
1076 analysis. Journal of Geochemical Exploration 112, 1-20.

1077 Giggenbach, W., 1997. The origin and evolution of fluids in magmatic-hydrothermal
1078 systems. Geochemistry of hydrothermal ore deposits.

1079 Giggenbach, W.F., Soto, R.C., 1992. Isotopic and chemical composition of water and
1080 steam discharges from volcanic-magmatic-hydrothermal systems of the Guanacaste
1081 Geothermal Province, Costa Rica. Applied Geochemistry 7, 309-332.

1082 Glazner, A.F., Bartley, J.M., Coleman, D.S., Gray, W., Taylor, R.Z., 2004. Are plutons
1083 assembled over millions of years by amalgamation from small magma chambers? GSA
1084 today 14, 4-12.

1085 Glodny, J., Kühn, A., Austrheim, H., 2008. Geochronology of fluid-induced eclogite and
1086 amphibolite facies metamorphic reactions in a subduction–collision system, Bergen Arcs,
1087 Norway. Contributions to Mineralogy and Petrology 156, 27-48.

1088 Hall, D.L., Sterner, S.M., Bodnar, R.J., 1988. Freezing point depression of NaCl-KCl-H
1089 2 O solutions. Economic Geology 83, 197-202.

1090 Hall, W., Schmidt, E., Howe, S., Broch, M., 1984. The Thompson Creek, Idaho,
1091 porphyry molybdenum deposit—an example of a fluorine-deficient molybdenum
1092 granodiorite system, International Association on the Genesis of Ore Deposits 6th
1093 Symposium, Tbilisi 1982, Proceedings, pp. 349-357.

1094 Haschke, M., Ahmadian, J., Murata, M., McDonald, I., 2010. Copper Mineralization
1095 Prevented by Arc-Root Delamination during Alpine-Himalayan Collision in Central Iran.
1096 Economic Geology 105, 855-865.

1097 Hassanpour, S., Alirezaei, S., Selby, D., Sergeev, S., 2014. SHRIMP zircon U–Pb and
1098 biotite and hornblende Ar–Ar geochronology of Sungun, Haftcheshmeh, Kighal, and
1099 Niaz porphyry Cu–Mo systems: evidence for an early Miocene porphyry-style
1100 mineralization in northwest Iran. International Journal of Earth Sciences 104, 45-59.

1101 Hassanzadeh, J., 1993. Metallogenic and tectono-magmatic events in the SE sector of the
1102 Cenozoic active continental margin of Iran (Shahr-e-Babak area, Kerman province). (Ph.
1103 D. Thesis). University of California.

1104 Hassanzadeh, J., Stockli, D.F., Horton, B.K., Axen, G.J., Stockli, L.D., Grove, M.,
1105 Schmitt, A.K., Walker, J.D., 2008. U-Pb zircon geochronology of late Neoproterozoic–
1106 Early Cambrian granitoids in Iran: Implications for paleogeography, magmatism, and
1107 exhumation history of Iranian basement. Tectonophysics 451, 71-96.

1108 Hawkesworth, C., Blake, S., Evans, P., Hughes, R., Macdonald, R., Thomas, L., Turner,
1109 S., Zellmer, G., 2000. Time scales of crystal fractionation in magma chambers—
1110 integrating physical, isotopic and geochemical perspectives. Journal of Petrology 41,
1111 991-1006.

1112 Heidari, S.M., Daliran, F., Paquette, J.-L., Gasquet, D., 2015. Geology, timing, and
1113 genesis of the high sulfidation Au (–Cu) deposit of Touzlar, NW Iran. Ore Geology
1114 Reviews 65, 460-486.

1115 Heidarzadeh, G., Ballato, P., Hassanzadeh, J., Ghassemi, M.R., Strecker, M.R., 2017.
1116 Lake overspill and onset of fluvial incision in the Iranian Plateau: Insights from the
1117 Mianeh Basin. Earth and Planetary Science Letters 469, 135-147.

1118 Heinhorst, J., Lehmann, B., Ermolov, P., Serykh, V., Zhurutin, S., 2000. Paleozoic
1119 crustal growth and metallogeny of Central Asia: evidence from magmatic-hydrothermal
1120 ore systems of Central Kazakhstan. Tectonophysics 328, 69-87.

1121 Hemley, J., Hunt, J., 1992. Hydrothermal ore-forming processes in the light of studies in
1122 rock-buffered systems; II, Some general geologic applications. Economic Geology 87,
1123 23-43.

1124 Hosseini, M.R., Hassanzadeh, J., Alirezaei, S., Sun, W., Li, C.-Y., 2017. Age revision of
1125 the Neotethyan arc migration into the southeast Urumieh-Dokhtar belt of Iran:
1126 Geochemistry and U–Pb zircon geochronology. Lithos 284-285, 296-309.

1127 Huang, R., Audétat, A., 2012. The titanium-in-quartz (TitaniQ) thermobarometer: A
1128 critical examination and re-calibration. Geochimica et Cosmochimica Acta 84, 75-89.

1129 Huber, H., 1977. Geological map of Iran at scale of 1: 1,000,000, National Iranian Oil
1130 Co., Tehran, Iran.

1131 Innocenti, F., Mazzuoli, R., Pasquare, G., Radicati di Brozolo, F., Villari, L., 1982.
1132 Tertiary and quaternary volcanism of the Erzurumkars area (Eastern Turkey):
1133 geochronological data and geodynamic evolution. Journal of Volcanology and
1134 Geothermal Research 13, 223-240.

1135 Ishihara, S., 1988. Rhenium contents of molybdenites in granitoid-series rocks in Japan.
1136 Economic Geology 83, 1047-1051.

1137 Iwano, H., Orihashi, Y., Hirata, T., Ogasawara, M., Danhara, T., Horie, K., Hasebe, N.,
1138 Sueoka, S., Tamura, A., Hayasaka, Y., 2013. An inter‐laboratory evaluation of OD‐3
1139 zircon for use as a secondary U–Pb dating standard. Island Arc 22, 382-394.

1140 Jamali, H., Mehrabi, B., 2015. Relationships between arc maturity and Cu–Mo–Au
1141 porphyry and related epithermal mineralization at the Cenozoic Arasbaran magmatic belt.
1142 Ore Geology Reviews 65, 487-501.

1143 Janković, S., 1982. Yugoslavia, in Dunning, F.W., Mykura, W., and Slater, D., eds.,
1144 Mineral deposits of Europe, v. 2, Southeast Europe: Institution of Mining and
1145 MetallurgyMineralogical Society, London, p. 143–202.

1146 Jochum, K.P., Weis, U., Stoll, B., Kuzmin, D., Yang, Q., Raczek, I., Jacob, D.E., Stracke,
1147 A., Birbaum, K., Frick, D.A., 2011. Determination of reference values for NIST SRM
1148 610–617 glasses following ISO guidelines. Geostandards and Geoanalytical Research 35,
1149 397-429.

1150 John, D., Ayuso, R., Barton, M., Blakely, R., Bodnar, R., Dilles, J., Gray, F., Graybeal,
1151 F., Mars, J., McPhee, D., 2010. Porphyry copper deposit model, chap. B of Mineral
1152 deposit models for resource assessment. US Geological Survey Scientific Investigations
1153 Report 2010, 1-169.

1154 John, D.A., Taylor, R.D., 2016. By-products of porphyry copper and molybdenum
1155 deposits: Chapter 7.

1156 Kananian, A., Sarjoughian, F., Nadimi, A., Ahmadian, J., Ling, W., 2014. Geochemical
1157 characteristics of the Kuh-e Dom intrusion, Urumieh–Dokhtar Magmatic Arc (Iran):

1158 Implications for source regions and magmatic evolution. Journal of Asian Earth Sciences
1159 90, 137-148.

1160 Kaszuba, J.P., Janecky, D.R., Snow, M.G., 2005. Experimental evaluation of mixed fluid
1161 reactions between supercritical carbon dioxide and NaCl brine: Relevance to the integrity
1162 of a geologic carbon repository. Chemical Geology 217, 277-293.

1163 Keith, J.D., Shanks, W.C., Archibald, D.A., Farrar, E., 1986. Volcanic and intrusive
1164 history of the Pine Grove porphyry molybdenum system, southwestern Utah. Economic
1165 Geology 81, 553-577.

1166 Keppler, H., Wyllie, P.J., 1991. Partitioning of Cu, Sn, Mo, W, U, and Th between melt
1167 and aqueous fluid in the systems haplogranite-H 2 O− HCl and haplogranite-H 2 O− HF.
1168 Contributions to Mineralogy and Petrology 109, 139-150.

1169 Kerr, A., van Nostrand, T., Dickson, W., Lynch, E., 2009. Molybdenum and tungsten in
1170 Newfoundland: a geological overview and a summary of recent exploration
1171 developments. Current Research, Newfoundland and Labrador Department of Natural
1172 Resources, Geological Survey, Report, 09-01.

1173 Khaleghi, F., Hosseinzadeh, G., Rasa, I., Moayyed, M., 2013. Geological and
1174 Geochemical Characteristics of the Syah Kamar Porphyry Molybdenum Deposit , West
1175 of Mianeh , NW Iran. ULUM-I ZAMIN 88, 187-196.

1176 Khodabandeh, A.A., Amini Azar, R., Faridi, M., 1999. Geological map of the Mianeh
1177 quadrangle. Geological Survey of Iran and Mining Exploration, Tehran.

1178 Kim, H., Yang, K., Lentz, D., Jeong, H.-Y., Kil, Y., Hwang, J., Park, S.-G., 2016. Low-
1179 salinity Liquid-rich or Vapor-like fluids in a porphyry-type Mo deposit, South Korea.
1180 The Canadian Mineralogist 54, 715-736.

1181 Kirkland, C., Smithies, R., Taylor, R., Evans, N., McDonald, B., 2015. Zircon Th/U
1182 ratios in magmatic environs. Lithos 212, 397-414.

1183 Kirsch, K., Navarre-Sitchler, A.K., Wunsch, A., McCray, J.E., 2014. Metal release from
1184 sandstones under experimentally and numerically simulated CO_2 leakage conditions.
1185 Environmental science & technology 48, 1436-1442.

1186 Klemm, L.M., Pettke, T., Heinrich, C.A., 2008. Fluid and source magma evolution of the
1187 Questa porphyry Mo deposit, New Mexico, USA. Mineralium Deposita 43, 533.

1188 Knight, C., Bodnar, R., 1989. Synthetic fluid inclusions: IX. Critical PVTX properties of
1189 NaCl-H2O solutions. Geochimica et Cosmochimica Acta 53, 3-8.

1190 Lawley, C., Richards, J., Anderson, R., Creaser, R., Heaman, L., 2010. Geochronology
1191 and geochemistry of the MAX porphyry Mo deposit and its relationship to Pb-Zn-Ag
1192 mineralization, Kootenay arc, southeastern British Columbia, Canada. Economic
1193 Geology 105, 1113-1142.

1194 Le Maitre, R.W., Streckeisen, A., Zanettin, B., Le Bas, M., Bonin, B., Bateman, P., 2005.
1195 Igneous rocks: a classification and glossary of terms: recommendations of the
1196 International Union of Geological Sciences Subcommission on the Systematics of
1197 Igneous Rocks. Cambridge University Press.

1198 Lions, J., Devau, N., De Lary, L., Dupraz, S., Parmentier, M., Gombert, P., Dictor, M.-
1199 C., 2014. Potential impacts of leakage from CO_2 geological storage on geochemical
1200 processes controlling fresh groundwater quality: a review. International Journal of
1201 Greenhouse Gas Control 22, 165-175.

1202 Little, M.G., Jackson, R.B., 2010. Potential impacts of leakage from deep CO_2
1203 geosequestration on overlying freshwater aquifers. Environmental science & technology
1204 44, 9225-9232.

1205 Liu, F., Lu, P., Griffith, C., Hedges, S.W., Soong, Y., Hellevang, H., Zhu, C., 2012. CO_2–
1206 brine–caprock interaction: Reactivity experiments on Eau Claire shale and a review of
1207 relevant literature. International Journal of Greenhouse Gas Control 7, 153-167.

1208 Liu, J., Mao, J.-W., Wu, G., Wang, F., Luo, D.-F., Hu, Y.-Q., 2015. Geochemical
1209 signature of the granitoids in the Chalukou giant porphyry Mo deposit in the
1210 Heilongjiang Province, NE China. Ore Geology Reviews 64, 35-52.

1211 Ludington, S., Hammarstrom, J., Piatak, N., 2009. Low-fluorine stockwork molybdenite
1212 deposits. US Geological Survey Open‐File Report 1211.

1213 Ludington, S., Plumlee, G.S., 2009. Climax-type porphyry molybdenum deposits. US
1214 Geological Survey.

1215 Ludwig, K., 2011. Isoplot v. 4.15: A Geochronological Toolkit for Microsoft Excel.
1216 Berkeley Geochronology Center Special Publication 4, 75.

1217 Mao, J., Wang, Y., Lehmann, B., Yu, J., Du, A., Mei, Y., Li, Y., Zang, W., Stein, H.J.,
1218 Zhou, T., 2006. Molybdenite Re–Os and albite 40Ar/39Ar dating of Cu–Au–Mo and
1219 magnetite porphyry systems in the Yangtze River valley and metallogenic implications.
1220 Ore Geology Reviews 29, 307-324.

1221 Mao, J.W., Pirajno, F., Xiang, J.F., Gao, J.J., Ye, H.S., Li, Y.F., Guo, B.J., 2011.
1222 Mesozoic molybdenum deposits in the east Qinling–Dabie orogenic belt: Characteristics
1223 and tectonic settings. Ore Geology Reviews 43, 264-293.

1224 Mao, J.W., Xie, G.Q., Bierlein, F., Qu, W.J., Du, A.D., Ye, H.S., Pirajno, F., Li, H.M.,
1225 Guo, B.J., Li, Y.F., Yang, Z.Q., 2008. Tectonic implications from Re–Os dating of
1226 Mesozoic molybdenum deposits in the East Qinling–Dabie orogenic belt. Geochimica et
1227 Cosmochimica Acta 72, 4607-4626.

1228 Massonne, H.-J., Opitz, J., Theye, T., Nasir, S., 2013. Evolution of a very deeply
1229 subducted metasediment from As Sifah, northeastern coast of Oman. Lithos 156, 171-
1230 185.

1231 McInnes, B., Evans, N., Belousova, E., Griffin, W., 2003. Porphyry copper deposits of
1232 the Kerman belt, Iran: timing of mineralization and exhumation processes. Sci. Res. Rep.
1233 Australia. CSIRO (41 pp).

1234 Mehrabi, B., Yardley, B., Cann, J., 1999. Sediment-hosted disseminated gold
1235 mineralisation at Zarshuran, NW Iran. Mineralium Deposita 34, 673-696.

1236 Mercer, C.N., Reed, M.H., Mercer, C.M., 2015. Time scales of porphyry Cu deposit
1237 formation: Insights from titanium diffusion in quartz. Economic Geology 110, 587-602.

1238 Mirnejad, H., Mathur, R., Hassanzadeh, J., Shafie, B., Nourali, S., 2013. Linking Cu
1239 mineralization to host porphyry emplacement: Re-Os ages of molybdenites versus U-Pb
1240 ages of zircons and sulfur isotope compositions of pyrite and chalcopyrite from the Iju
1241 and Sarkuh porphyry deposits in Southeast Iran. Economic Geology 108, 861-870.

1242 Mirnejad, H., Simonetti, A., Molasalehi, F., 2011. Pb isotopic compositions of some Zn–
1243 Pb deposits and occurrences from Urumieh–Dokhtar and Sanandaj–Sirjan zones in Iran.
1244 Ore Geology Reviews 39, 181-187.

1245 Moghadam, H.S., Rossetti, F., Lucci, F., Chiaradia, M., Gerdes, A., Martinez, M.L.,
1246 Ghorbani, G., Nasrabady, M., 2016. The calc-alkaline and adakitic volcanism of the
1247 Sabzevar structural zone (NE Iran): implications for the Eocene magmatic flare-up in
1248 Central Iran. Lithos 248, 517-535.

1249 Moritz, R., Ghazban, F., Singer, B.S., 2006. Eocene gold ore formation at Muteh,
1250 Sanandaj-Sirjan tectonic zone, Western Iran: a result of late-stage extension and
1251 exhumation of metamorphic basement rocks within the Zagros Orogen. Economic
1252 Geology 101, 1497-1524.

1253 Moritz, R., Rezeau, H., Ovtcharova, M., Tayan, R., Melkonyan, R., Hovakimyan, S.,
1254 Ramazanov, V., Selby, D., Ulianov, A., Chiaradia, M., Putlitz, B., 2016. Long-lived,
1255 stationary magmatism and pulsed porphyry systems during Tethyan subduction to post-
1256 collision evolution in the southernmost Lesser Caucasus, Armenia and Nakhitchevan.
1257 Gondwana Research 37, 465-503.

1258 Müller, A., Herklotz, G., Giegling, H., 2018. Chemistry of quartz related to the
1259 Zinnwald/Cínovec Sn-W-Li greisen-type deposit, Eastern Erzgebirge, Germany. Journal
1260 of Geochemical Exploration 190, 357-373.

1261 Nabatian, G., Li, X.-H., Wan, B., Honarmand, M., 2017a. The genesis of Mo-Cu deposits
1262 and mafic igneous rocks in the Senj area, Alborz magmatic belt, Iran. Mineralogy and
1263 Petrology, 1-20.

1264 Nabatian, G., Wan, B., Honarmand, M., 2017b. Whole rock geochemistry, molybdenite
1265 Re-Os geochronology, stable isotope and fluid inclusion investigations of the Siah-
1266 Kamar deposit, western Alborz-Azarbayjan: New constrains on the porphyry Mo deposit
1267 in Iran. Ore Geology Reviews 91, 638-659.

1268 Nabavi, M.H., 1976. An introduction to the geology of Iran. Geological survey of Iran
1269 109.

1270 Newberry, R., 1979. Polytypism in molybdenite (I); A non-equilibrium impurity-induced
1271 phenomenon. American Mineralogist 64, 758-767.

1272 Ni, P., Wang, G.-G., Yu, W., Chen, H., Jiang, L.-L., Wang, B.-H., Zhang, H.-D., Xu, Y.-
1273 F., 2015. Evidence of fluid inclusions for two stages of fluid boiling in the formation of
1274 the giant Shapinggou porphyry Mo deposit, Dabie Orogen, Central China. Ore Geology
1275 Reviews 65, 1078-1094.

1276 NICICO, 2009a. Geological report and map of Goydaraq area, at scale of 1:25000,
1277 Internal report.

1278 NICICO, 2009b. Geological report and map of Khatoon-Abad area, at scale of 1:25000,
1279 Internal report.

1280 NICICO, 2009c. Geological report and map of Siah-Kamar area, at scale of 1:25000,
1281 Internal report.

1282 NICICO, 2010. Geological report and map of Siah-Kamar area, at scale of 1:5000,
1283 Internal report.

1284 Oliver, N.H., Bons, P.D., 2001. Mechanisms of fluid flow and fluid–rock interaction in
1285 fossil metamorphic hydrothermal systems inferred from vein–wallrock patterns,
1286 geometry and microstructure. Geofluids 1, 137-162.

1287 Pettke, T., Oberli, F., Heinrich, C.A., 2010. The magma and metal source of giant
1288 porphyry-type ore deposits, based on lead isotope microanalysis of individual fluid
1289 inclusions. Earth and Planetary Science Letters 296, 267-277.

1290 Rezeau, H., Moritz, R., Wotzlaw, J.-F., Tayan, R., Melkonyan, R., Ulianov, A., Selby,
1291 D., d'Abzac, F.-X., Stern, R.A., 2016. Temporal and genetic link between incremental
1292 pluton assembly and pulsed porphyry Cu-Mo formation in accretionary orogens. Geology
1293 44, 627-630.

1294 Richards, J.P., 2015. Tectonic, magmatic, and metallogenic evolution of the Tethyan
1295 orogen: From subduction to collision. Ore Geology Reviews 70, 323-345.

1296 Richards, J.P., Sholeh, A., 2016. The Tethyan tectonic history and Cu-Au metallogeny of
1297 Iran, Tectonics and Metallogeny of the Tethyan Orogenic Belt, Society of Economic
1298 Geologists Special Publication, pp. 193-212.

1299 Richards, J.P., Wilkinson, D., Ullrich, T., 2006. Geology of the Sari Gunay epithermal
1300 gold deposit, northwest Iran. Economic Geology 101, 1455-1496.

1301 Rives, T., Rawnsley, K., Petit, J.-P., 1994. Analogue simulation of natural orthogonal
1302 joint set formation in brittle varnish. Journal of Structural Geology 16, 419-429.

1303 Robb, L., 2004. Introduction to ore-forming processes. Blackwell publishing.

1304 Rolland, Y., 2017. Caucasus collisional history: Review of data from East Anatolia to
1305 West Iran. Gondwana Research 49, 130-146.

1306 Rossetti, F., Tecce, F., Billi, A., Brilli, M., 2007. Patterns of fluid flow in the contact
1307 aureole of the Late Miocene Monte Capanne pluton (Elba Island, Italy): the role of
1308 structures and rheology. Contributions to Mineralogy and Petrology 153, 743-760.

1309 Rubatto, D., 2002. Zircon trace element geochemistry: partitioning with garnet and the
1310 link between U–Pb ages and metamorphism. Chemical Geology 184, 123-138.

1311 Sarjoughian, F., Kananian, A., 2017. Zircon U-Pb geochronology and emplacement
1312 history of intrusive rocks in the Ardestan section, central Iran. Geologica acta 15, 0025-
1313 0036.

1314 Sarjoughian, F., Kananian, A., Haschke, M., Ahmadian, J., Ling, W., Zong, K., 2012.
1315 Magma mingling and hybridization in the Kuh-e Dom pluton, Central Iran. Journal of
1316 Asian Earth Sciences 54-55, 49-63.

1317 Seedorff, E., Dilles, J.H., Proffett, J.J.M., Einaudi, M.T., Zurcher, L., Stavast, W.J.A.,
1318 Johnson, D.A., Barton, M.D., 2005. Porphyry Deposits: Characteristics and Origin of
1319 Hypogene Features, In: Hedenquist, J.W., Thompson, J.F.H., Goldfarb, R.J., Richards,
1320 J.P. (Eds.), One Hundredth Anniversary Volume. Society of Economic Geologists.

1321 Seedorff, E., Einaudi, M.T., 2004. Henderson porphyry molybdenum system, Colorado:
1322 II. Decoupling of introduction and deposition of metals during geochemical evolution of
1323 hydrothermal fluids. Economic Geology 99, 39-72.

1324 Selby, D., Creaser, R.A., 2001. Re-Os geochronology and systematics in molybdenite
1325 from the Endako porphyry molybdenum deposit, British Columbia, Canada. Economic
1326 Geology 96, 197-204.

1327 Selby, D., Creaser, R.A., 2004. Macroscale NTIMS and microscale LA-MC-ICP-MS Re-
1328 Os isotopic analysis of molybdenite: Testing spatial restrictions for reliable Re-Os age
1329 determinations, and implications for the decoupling of Re and Os within molybdenite.
1330 Geochimica et Cosmochimica Acta 68, 3897-3908.

1331 Selby, D., Nesbitt, B.E., Muehlenbachs, K., Prochaska, W., 2000. Hydrothermal
1332 alteration and fluid chemistry of the Endako porphyry molybdenum deposit, British
1333 Columbia. Economic Geology 95, 183-202.

1334 Seo, J.H., Guillong, M., Heinrich, C.A., 2012. Separation of molybdenum and copper in
1335 porphyry deposits: The roles of sulfur, redox, and pH in ore mineral deposition at
1336 Bingham Canyon. Economic Geology 107, 333-356.

1337 Shafiei, B., Haschke, M., Shahabpour, J., 2009. Recycling of orogenic arc crust triggers
1338 porphyry Cu mineralization in Kerman Cenozoic arc rocks, southeastern Iran.
1339 Mineralium Deposita 44, 265.

1340 Shafiei, B., Shahabpour, J., Haschke, M., 2008. Transition from Paleogene normal calc-
1341 alkaline to Neogene adakitic-like plutonism and Cu-metallogeny in the Kerman porphyry
1342 copper belt: response to Neogene crustal thickening. Journal of Sciences, Islamic
1343 Republic of Iran 19, 67-84.

1344 Shahabpour, J., Kramers, J., 1987. Lead isotope data from the Sar-Cheshmeh porphyry
1345 copper deposit, Iran. Mineralium Deposita 22, 278-281.

1346 Shahsavari Alavijeh, B., Rashidnejad-Omran, N., Corfu, F., 2017. Zircon U-Pb ages and
1347 emplacement history of the Nodoushan plutonic complex in the central Urumieh-Dokhtar
1348 magmatic belt, Central Iran: Product of Neotethyan subduction during the Paleogene.
1349 Journal of Asian Earth Sciences 143, 283-295.

1350 Shannon, J., Walker, B., Carten, R., Geraghty, E., 1982. Unidirectional solidification
1351 textures and their significance in determining relative ages of intrusions at the Henderson
1352 Mine, Colorado. Geology 10, 293-297.

1353 Shinohara, H., Kazahaya, K., Lowenstern, J.B., 1995. Volatile transport in a convecting
1354 magma column: Implications for porphyry Mo mineralization. Geology 23, 1091-1094.

1355 Sillitoe, R.H., 2010. Porphyry copper systems. Economic Geology 105, 3-41.

1356 Simmonds, V., Moazzen, M., 2015. Re–Os dating of molybdenites from Oligocene Cu–
1357 Mo–Au mineralized veins in the Qarachilar area, Qaradagh batholith (northwest Iran):
1358 implications for understanding Cenozoic mineralization in South Armenia, Nakhchivan,
1359 and Iran. International Geology Review 57, 290-304.

1360 Simmonds, V., Moazzen, M., Selby, D., 2017. Re-Os dating of mineralization in Siah
1361 Kamar porphyry Mo deposit (NW Iran) and investigating on its temporal relationship
1362 with porphyry Cu-Mo deposits in the southern Lesser Caucasus, NW and central Iran,
1363 EGU General Assembly Conference Abstracts, p. 665.

1364 Simmonds, V., Moazzen, M., Selby, D., 2019. U-Pb zircon and Re-Os molybdenite age
1365 of the Siah Kamar porphyry molybdenum deposit, NW Iran. International Geology
1366 Review, 1-17.

1367 Sinclair, W., 2007. Porphyry deposits. Mineral deposits of Canada: A synthesis of major
1368 deposit-types, district metallogeny, the evolution of geological provinces, and exploration
1369 methods: Geological Association of Canada, Mineral Deposits Division, Special
1370 Publication 5, 223-243.

1371 Smoliar, M.I., Walker, R.J., Morgan, J.W., 1996. Re-Os ages of group IIA, IIIA, IVA,
1372 and IVB iron meteorites. Science 271, 1099-1102.

1373 Stein, H., Markey, R., Morgan, J., Hannah, J., Scherstén, A., 2001. The remarkable Re–
1374 Os chronometer in molybdenite: how and why it works. Terra Nova 13, 479-486.

1375 Stocklin, J., 1968. Structural history and tectonics of Iran: a review. AAPG Bulletin 52,
1376 1229-1258.

1377 Sutulov, A., 1973. Mineral resources and the economy of the USSR. Backbeat Books.

1378 Taghipour, N., Aftabi, A., Mathur, R., 2008. Geology and Re-Os Geochronology of
1379 Mineralization of the Miduk Porphyry Copper Deposit, Iran. Resource Geology 58, 143-
1380 160.

1381 Taylor, R.D., Hammarstrom, J.M., Piatak, N.M., Seal II, R.R., 2012. Arc-related
1382 porphyry molybdenum deposit model: Chapter D in Mineral deposit models for resource
1383 assessment. US Geological Survey.

1384 Ulrich, T., Mavrogenes, J., 2008. An experimental study of the solubility of molybdenum
1385 in H_2O and KCl–H_2O solutions from 500 °C to 800 °C, and 150 to 300 MPa. Geochimica
1386 et Cosmochimica Acta 72, 2316-2330.

1387 Verdel, C., Wernicke, B.P., Hassanzadeh, J., Guest, B., 2011. A Paleogene extensional
1388 arc flare-up in Iran. Tectonics 30.

1389 Villa, I.M., De Bièvre, P., Holden, N., Renne, P., 2015. IUPAC-IUGS recommendation
1390 on the half life of 87Rb. Geochimica et Cosmochimica Acta 164, 382-385.

1391 Wallace, S., 1995. The Climax-type molybdenite deposits: what they are, where they are
1392 and why they are. Economic Geology 90, 1359-1380.

1393 Wan, B., Deng, C., Najafi, A., Hezareh, M.R., Talebian, M., Dong, L., Chen, L., Xiao,
1394 W., 2018. Fertilizing porphyry Cu deposits through deep crustal hot zone melting.
1395 Gondwana Research 60, 179-185.

1396 Wang, G., Wu, G., Xu, L., Li, X., Zhang, T., Quan, Z., Wu, H., Li, T., Liu, J., Chen, Y.,
1397 2017. Molybdenite Re–Os age, H–O–C–S–Pb isotopes, and fluid inclusion study of the
1398 Caosiyao porphyry Mo deposit in Inner Mongolia, China. Ore Geology Reviews 81, 728-
1399 744.

1400 Wark, D.A., Watson, E.B., 2006. TitaniQ: a titanium-in-quartz geothermometer.
1401 Contributions to Mineralogy and Petrology 152, 743-754.

1402 Westra, G., Keith, S.B., 1981. Classification and genesis of stockwork molybdenum
1403 deposits. Economic Geology 76, 844-873.

1404 Whitcher, I., 1975. Anduramba molybdenum prospect, Economic Geology of Australia
1405 and Papua New Guinea. 1—Metals, pp. 793-794.

1406 Whitney, D.L., Evans, B.W., 2010. Abbreviations for names of rock-forming minerals.
1407 American Mineralogist 95, 185-187.

1408 Wiedenbeck, M., Alle, P., Corfu, F., Griffin, W., Meier, M., Oberli, F.v., Quadt, A.v.,
1409 Roddick, J., Spiegel, W., 1995. Three natural zircon standards for U−Th−Pb, Lu−Hf,
1410 trace element and REE analyses. Geostandards Newsletter 19, 1-23.

1411 Wilkinson, J., 2001. Fluid inclusions in hydrothermal ore deposits. Lithos 55, 229-272.

1412 Wilkinson, J.J., 2013. Triggers for the formation of porphyry ore deposits in magmatic
1413 arcs. Nature Geoscience 6, 917-925.

1414 Wu, Y.-S., Chen, Y.-J., Zhou, K.-F., 2017. Mo deposits in Northwest China: Geology,
1415 geochemistry, geochronology and tectonic setting. Ore Geology Reviews 81, 641-671.

1416 Xiaoyun, C., 1989. Solubility of molybdenite and the transport of molybdenum in
1417 hydrothermal solutions. Ph. D. thesis. Iowa State University, 1~ 111.

1418 Xue, C., Chi, G., Zhao, X., Wu, G., Zhao, Z., Dong, L., 2016. Multiple and prolonged
1419 porphyry Cu–Au mineralization and alteration events in the Halasu deposit, Chinese
1420 Altai, Xinjiang, northwestern China. Geoscience Frontiers 7, 799-809.

1421 Yang, Z., 2007. Re-Os isotopic ages of Tangjiaping molybdenum deposit in Shangcheng
1422 County, Henan and their geological significance. Kuangchuang Dizhi(Mineral Deposits)
1423 26, 289-295.

1424 Yeganehfar, H., Ghorbani, M.R., Shinjo, R., Ghaderi, M., 2013. Magmatic and
1425 geodynamic evolution of Urumieh–Dokhtar basic volcanism, Central Iran: major, trace
1426 element, isotopic, and geochronologic implications. International Geology Review 55,
1427 767-786.

1428 Zeng, Q.-D., Sun, Y., Chu, S.-X., Duan, X.-X., Liu, J., 2015. Geochemistry and
1429 geochronology of the Dongshanwan porphyry Mo–W deposit, Northeast China:
1430 implications for the Late Jurassic tectonic setting. Journal of Asian Earth Sciences 97,
1431 472-485.

1432 Zeng, Q., Liu, J., Chu, S., Wang, Y., Sun, Y., Duan, X., Zhou, L., 2012. Mesozoic
1433 molybdenum deposits in the East Xingmeng orogenic belt, northeast China:
1434 characteristics and tectonic setting. International Geology Review 54, 1843-1869.

1435 Zhai, D., Liu, J., Tombros, S., Williams-Jones, A.E., 2017. The genesis of the Hashitu
1436 porphyry molybdenum deposit, Inner Mongolia, NE China: constraints from
1437 mineralogical, fluid inclusion, and multiple isotope (H, O, S, Mo, Pb) studies.
1438 Mineralium Deposita 53, 377-397.

1439 Zhang, X., Lentz, D.R., Yao, C., Liu, R., Yang, Z., Mei, Y., Fan, X., Huang, F., Qin, Y.,
1440 Zhang, K., 2018. Geochronology, geochemistry, and Sr–Nd–Pb–Hf isotopes of the
1441 Zhunsujihua granitoid intrusions associated with the molybdenum deposit, northern Inner
1442 Mongolia, China: implications for petrogenesis and tectonic setting. International Journal
1443 of Earth Sciences 107, 687-710.

1444 Zhang, Y.-G., Frantz, J.D., 1987. Determination of the homogenization temperatures and
1445 densities of supercritical fluids in the system NaClKClCaCl$_2$H$_2$O using synthetic fluid
1446 inclusions. Chemical Geology 64, 335-350.

1447 Zindler, A., Hart, S., 1986. Chemical geodynamics. Annual review of earth and planetary
1448 sciences 14, 493-571.

1449

1450 ## Figures captions

1451 Figure 1: Simplified tectono-geological map of Iran with the main Cu, Au and Mo ore
1452 deposits and their ages. Based on maps from the (Huber, 1977), with additional information
1453 from (Berberian and King, 1981) and Richards et al. (2012). See also Table 1 for the
1454 references for each mineralisation site.

1455 Figure 2: Simplified geological map of Mianeh-Hashtroud region, as derived from field
1456 and remote sensing investigations (modified after Amidi et al., 1987; NICICO, 2009c, b, a).

1457 Figure 3: Top: Geological-alteration map of the Siah-Kamar Mo deposit (see Fig. 3 for
1458 map location). The ellipse indicates the estimated alteration zone. Bottom: Interpretative
1459 geological cross section across the Mo ore deposit, also showing distribution of the main
1460 alteration types. Abbreviations: Ab, Albite; Act, Actinolite; Ap, Apatite; Bt, Biotite, Cal,
1461 Calcite; Chl, Chlorite; Ep, Epidote; ill, Illite. Kal, Kaolinite; Kfs, K-feldspar; Mag,
1462 Magnetite; Or, Orthose, Psp, Paraspurite; Po, Pyrrhotite; Py, Pyrite; Qtz, Quartz; Sch,
1463 Scheelite; Ser, Sericite.

1464 Figure 4: General field view of the Siah-Kamar Mo deposit area (field of view 2.5 km).
1465 The line drawing illustrates the main rock and alteration types. Abbreviations: alt., alteration;
1466 Cb, carbonate; K, Potassic; mp, mineralized basic/intermediate porphyry rocks.

1467 Figure 5: Rock textures and alterations. (a) The textural appearance of the potassic-sodic
1468 alteration within the main mineralised porphyry body in the outcrop. Alteration mineralogy
1469 consists of Bt-Fsp+ Po, Mg assemblage overprinting early igneous phases. (b) potassic-sodic
1470 alteration at the thin section scale (plane polarised light). (c) Back-scattered electron (BSE)
1471 image showing disseminated molybdenite flakes within the secondary feldspar-biotite
1472 assemblage. (d) Biotite veinlets in the potassic-sodic alteration zone overprinted by Kfs-Qz
1473 veins (plane polarised light). (e) BSE image showing early magnetite inclusions in secondary
1474 feldspar and ilmenite inclusions in texturally-late biotite. (f) Brecciated andesite country
1475 rocks and epidote veining within the propylitic alteration zone. (g) General appearance of the
1476 phyllic and argillic alteration zones. (h) Rock slab from phyllic/silicified zones showing the
1477 development of Qz + Py veins with sericitic halos; (i-j) Microtexture of volcanic country rock
1478 within pronounced phyllic alteration made of Qz + Ser + Py assemblage (crossed polars).

1479

1480 Figure 6: (a) The contact between the mineralised porphyry body and the country rocks.
1481 Note the presence of potassic alteration and intense veining within the porphyry body and
1482 how the veining dies out abruptly across the contact (see also the interpretative line drawing
1483 in the inset). (b) Rose diagram of the cumulative vein strikes as measured within the different
1484 alteration zones. (c) Contour diagram of the cumulative poles to Mo-mineralised veins (V2a
1485 and V2b) within the potassic-sodic alteration zone (Equal area Schmidt net, lower

1486 hemisphere projection). (d) Contour diagram of the poles to (V2b) Cb-Mo veins within the
1487 potassic-sodic alteration zone (Equal area Schmidt net, lower hemisphere projection). (e)
1488 Contour diagram of the poles to epidote (Ep) veins within the propylitic alteration zone
1489 (Equal area Schmidt net, lower hemisphere projection).

1490 Figure 7. Conceptual model for veining and Mo mineralisation within the potassic-sodic
1491 alteration zone (see text for further details).

1492 Figure 8. (a) Rock slab of an early Qz-Kfs-Ab V2a vein with V2b Mol-bearing carbonate
1493 mineral assemblages growing in pre-existing vugs. Note the marginal K-feldspar + albite
1494 selvage. (b) BSE image showing the textural appearance of a V2a Qz-Kfs vein overprinted by
1495 a late, post-ore Fe-oxide vein. Molybdenite occurs in the centre of the vein. (c) BSE image
1496 showing coexisting scheelite (Sch) and Mol within V2a Qz + Kfs vein.

1497 Figure 9. (a) Rock slabs of composite V2a-V2b veins showing different degree of the
1498 textural overprinting operated by the Cb-Mol mineralisation. (b) BSE image showing V2b
1499 veining overprinting early V2a Qz, sericite halos and compositional zoning in Cb. (c) BSE
1500 image showing a ribbon texture along margins of a V2b vein, attesting episodic Cb-Mol
1501 precipitation. (d) BSE image showing the textural overprint operated by the V2b Cb-Mo
1502 veining onto pre-existing Qz-Kfs V2a one. Sericite formed after alteration of Kfs. Note the
1503 reworking of the Qz grain boundary during V2b veining.

1504 Figure10: Mineralization stages and their associated mineral assemblages in the SKMD.

1505 Figure 11. Representative discrimination diagrams for quartz chemistry (after Müller et
1506 al., 2018) as derived from in situ LA-ICPMS analyses of quartz grains from V2a veins. (a) Li
1507 vs Al. (b) Al vs Ge. (c) Al vs Li.

1508 Figure 12: Microphotographs of the fluid inclusions types hosted in V2a-V2b veins. (a)
1509 Type A1 (two-phase L-rich) fluid inclusions in Qz (V2a vein). (b) Type A2 (two-phase L-
1510 rich) fluid inclusions in Qz (V2a vein). (c) Type A3 (two-phase L-rich) fluid inclusions in
1511 Qz-Py vein from the phyllic alteration zone. (d) Type A4 (two-phase L-rich) fluid inclusions
1512 in Psp (V2b Vein). Type B solid-bearing fluid inclusions in Qz (V2a vein).

1513 Figure 13. (a) and (b) Representative Raman spectra from fluid and gas phases from
1514 types A1 fluid inclusions in Qz from V2a veins.

1515 Figure 14. Histogram of homogenization temperature (Th) (a) and salinity (b) for the
1516 analysed fluid inclusion types.

1517 Figure 15. (a, c, e and g) Cathodoluminescence images from the analysed zircon grains,
1518 with location of the laser spots (circles and relative id numbers in parenthesis) and obtained
1519 $^{206}Pb/^{238}U$ ages (2σ error; Ma). Spots that provided inherited zircon ages are denoted by
1520 dashed circles. (b) Tera-Wasserburg concordia diagram for sample MN03 (d, f, h).
1521 Conventional Concordia diagrams with Concordia ages indicated (2σ error; Ma) for the
1522 MN01, MN19, and MN31 samples. See also Table 5 for the corresponding analytical results.

1523 Fig 16: Mineral data and Rb–Sr age results for sample MN02. Analytical data are given
1524 in Table 7. Grain size is indicated when different grain size fractions were analyzed. Kfs, K-
1525 feldspar.

1526 Figure 17: (a) Calculated Isochores for the representative type-A1 (quartz) and -A4
1527 (paraspurrite) fluid inclusions (BULK and ISOC software; Bakker, 2003), combined with
1528 isopleths as obtained from Ti-in-quartz thermometry. (b) Salinity versus homogenization
1529 temperature (Th) diagram for all the FI types. Dashed arrows indicate the possible fluid
1530 evolution. (c) Schematic diagram showing typical trends in a Th-salinity space for fluid
1531 evolution in hydrothermal ore deposits (after Wilkinson, 2001).

1532 Figure 18: (a) A model for the Mo mineralisation at Siah-kamar framed within a scenario
1533 of long-lived thermal anomaly and magmatism. (a) Stage-1 mineralisation (33Ma).
1534 Emplacement of the basic/intermediate porphyry body with pervasive potassic-sodic
1535 alteration and low-grade disseminated Mo mineralization. (b) Emplacement of a new batch of
1536 acidic magmas (at 29-28 Ma) caused re-fertilisation of the intrusive/cap rock system, with
1537 formation of V2a veining (stage-2a). (c) The main mineralisation stage (29-28 Ma). The
1538 continuous exsolution of acidic, CO2-bearing fluid from the new magma products caused
1539 leaching of the early deposited Mo and, by neutralisation due to the interaction with meteoric
1540 fluids, the high-grade Mo mineralization during structurally-controlled stockwork Cb veining
1541 (stage-2b).

1542

1543 Table 1. List of the studied samples with their location, petrographical characteristic and
1544 analytical methods adopted.

S	Ro	Rock texture and	Alteration	Locati	Method

amp le	ck Type	petrography	type	on (decimal degree)	EPMA	LA-	Zircon	Mol.	Rb-Sr
M N01	Rh yolitoi d	Porphyritic with microgranular groundmass. Qz (5-10 %), Pl+Kfs (5-10 %) phenocrysts. Groundmass: Qz (20-30 %), KFsp (40-50 %), Pl (10-15 %), Biotite (<5 %).	Weakly phyllic alteration. Qz veins, rare Ser, Py and Fe-oxides	N: 37.41297 E: 47.59745					
M N02 MN 03	A ndesit oid/Ba saltoid (Diorit e to monzo diorite porphy ry)	Porphyritic with microgranular groundmass. Magmatic texture mostly overprinted. Relic Pl (20-30 %) phenocrysts and pseudomorphous secondary aggregates after Cpx (5-10 %).	Strong sodic-potassic alteration. Disseminated secondary fine grained Ab+Kfs+Qtz+ Bt+Mag (40-50%), Qz-Afs-Mol-Cb-Rt-Sch veins (5-10 %)	N: 37.39916 E: 47.59519		*			
M N19	Da citoid	Porphyritic with glassy groundmass. Glass (50-60 %), euhedral to subhedral Pl (20-25 %), Bt (5-7 %), Amph (2-3 %), Qz (5-7 %) phenocrysts.	Almost unaltered; secondary Chl on Amph	N: 37.39925 E: 47.58888					

MN31	Andesitoid/Basaltoid (Diorite to monzodiorite porphyry)	Porphyritic with microgranular groundmass. Pl (30-35 %), Cpx (15-20 %) phenocrysts. Groudnmass: Pl (25-30 %), Cpx (15-20 %)+ Mag (4-6 %),	Propylitic alteration. Ep (10-15 %)+ Act/Tr (5-10 %), Py	N: 37.38710 E: 47.60161
MN65	Andesitoid/Basaltoid (monzodiorite)	Porphyritic with microgranular groundmass. Pl (20-30 %), Cpx (7-10 %), Opx (5 %) phenocrysts. Groundmass: Pl+KFs+Px+Mag (40-50 %)	Weakly propylitic alteration. Cb (disseminated over mafic minerals and Pl) and Cb veining (2-3 %), secondary Chl on Cpx and Opx.	N: 37.406533 E: 47.589648
MN55	Andesitoid/Basaltoid (monzonite porphyry)	Porphyritic with microgranular groundmass. Pl (5-7 %) phenocrysts. Groudnmass: Pl (60-70), KFs (5-10? %), Mag (5-7 %).	Weakly altered to Cb	N: 37.40281 E: 47.59006

1545 **15.**

1547 Table 2. Trace element chemistry of quartz from V2 veins

Spot	Li	B	Al	Mn	Ga	Ge	As
	ppm						
v4q	3.26	3.90	35.97	0.15	0.10	0.89	0.01
v4a2	24.52	5.18	15 6.97	1.05	0.11	1.41	2.02
v4b2	3.34	3.57	98.49	0.70	0.13	1.20	1.77
v4c2	6.50	8.35	89.96	0.27	0.01	1.98	0.94
v4d2	28.03	7.63	16 0.22	0.20	0.06	1.87	0.80
v4e2	1.86	4.58	45.10	0.24	*dl*	*dl*	0.14
v4f2	17.07	4.00	10 2.47	0.66	0.17	1.33	*dl*

bdl: Below detection limit

1548

1549 **16.**

1551 Table 3. Ti-in-Quartz content and results of TitaniQ thermometry (V2 veins)

Spot	Ti (ppm)	Temperature (°C) calculated for P (kbar)				
		0.5	*1*	*1.5*	*2*	*2.5*
v4b	21.17	494	527	550	569	585
v4c	21.52	495	528	551	570	586
v4d	31.88	527	561	585	605	621
v4e	29.78	521	555	579	599	615
v4f	17.42	479	511	534	553	568
v4g	44.20	555	591	616	636	653
v4i	45.00	557	592	618	638	655
v4j	20.91	493	526	549	568	583
v4n	44.69	556	592	617	637	654
v4q	17.36	479	511	534	552	568
v4a2	54.65	575	611	637	657	675
v4b2	41.66	550	585	610	630	647

v	24.5	5	5	5	5	5
4c2	7	05	39	63	81	98
v	48.0	5	5	6	6	6
4d2	2	63	98	24	44	61
v	23.6	5	5	5	5	5
4e2	1	02	36	59	78	94
v	24.6	5	5	5	5	5
4f2	7	06	39	63	82	98

1552

1554 Table 4. Summary of the FI characteristics and the obtained microthermometry results

Type	V to L ratio	Host mineral	Alteration zone	Measured number	T freezing (°C)	T eutectic (°C)	T homogenization (°C)	T melting (°C)	Salinity (wt.% NaCl eq.)
Type A1 (L-rich+V)	0.5-1	Quartz	Potassic	44	-44.4 to -29.6 (Mean=-38.5)	-30 to -22.5 (Mean=-25.3)	298 to 365 (Mean=333)	-4,3 to -0,6 (Mean=-2)	1 to 6,9 (Mode=3.85)
Type A2 (L-rich+V)	0.1-0.4	Quartz	Potassic	195	-47.2 to -25.3 (Mean=-39)	-31.5 to -23 (Mode=-23)	170 to 352 (Mean=272)	-3.7 to -0.1 (Mean=-1.5)	0.2 to 6 (Mean=2.6)
Type A3 (L-rich+V)	0.2-0.4	Quartz	Phyllic	52	-41.4 to -31 (Mean=-33.6)	-22 to -21 (Mean=-21.5)	232 to 365 (Mode=320)	-2,6 to -1 (Mean=-1.8)	1.7 to 4.3 (Mean=3.1)
Type A4 (L-rich+V)	0.1-.25	Paraspurrite	Potassic	91	-30 to -42 (Mean=-39)	-24 to -33 (Mean=-27)	145 to 300 (Mode=225)	-1,2 to -0,1 (Mean=-0.35)	0.2 to 2.1 (Mean=0.6)

Type B (L-rich+ V±S)	0.1-0.2	Quartz	Potassic	4	-80 to -39.8	-25 to -65 (Mean= -28.5 and -61)	203 to 320	-34 to -11.5	3 0.5 to 32

1555

1557 Table 5. Results of LA–ICP–MS U-(Th)-Pb zircon data.

MN01; Northing: 37.41297, Easting: 47.59745										
MN03; Northing: 37.39916, Easting: 47.59519										
MN19; Northing: 37.39925, Easting: 47.58888										
MN31; Northing: 37.38710, Easting: 47.60161										

1558 * 206 Percentage of Pb contributed by common Pb on the basis of 204 Pb. Value of common Pb was assumed by Stacey and Kramers (1975) model; n.d.: no detection of 204Pb

1559 ** Degree of discordance (%); negative numbers and blanks show normal discordant and concordanct within 2σ of the analytical error, respectively.

1561 Table 6. Re-Os isotopic data for two molybdenite samples from the Siah-Kamar Mo deposit

Sample	wt (g)	Re(ppm)		^{187}Re(ppm)		^{187}Os(ppb)		Age	*	#
RO780-13_Mo1B	0.016	19.33	0.09	12.15	0.05	5.81	0.02	2 8.70	0.14	0.17
RO780-14_Mo2B	0.016	22.14	0.10	13.92	0.06	6.56	0.03	2 8.29	0.14	0.16

1562 *uncertainty including all sources of analytical uncertainty

1563 #uncertainty including all sources of analytical uncertainty plus decay constant

1565 Table 7. Rb-Sr analytical data for the mineral separated from sample MN02

Analysis	material	Rb ppm	Sr ppm	$^{87}Rb/^{86}Sr$	$^{87}Sr/^{86}Sr$	$^{87}Sr/^{86}Sr$ $2\sigma_m$ (%)
PS3104	biotite	306	194	4.564	0.707085	0.0019
PS3105	kfsp >160 µm	138	875	0.455	0.705176	0.0011
PS3106	sericite >125 µm	397	118	9.732	0.708913	0.0015
PS3107	kfsp <160 µm	145	893	0.471	0.705179	0.0008
PS3108	sericite <125 µm	375	190	5.72	0.707161	0.0022
PS3109	apatite conc.	91.2	652	0.405	0.705162	0.0021

1566

1567

1568

1569

1570

1571

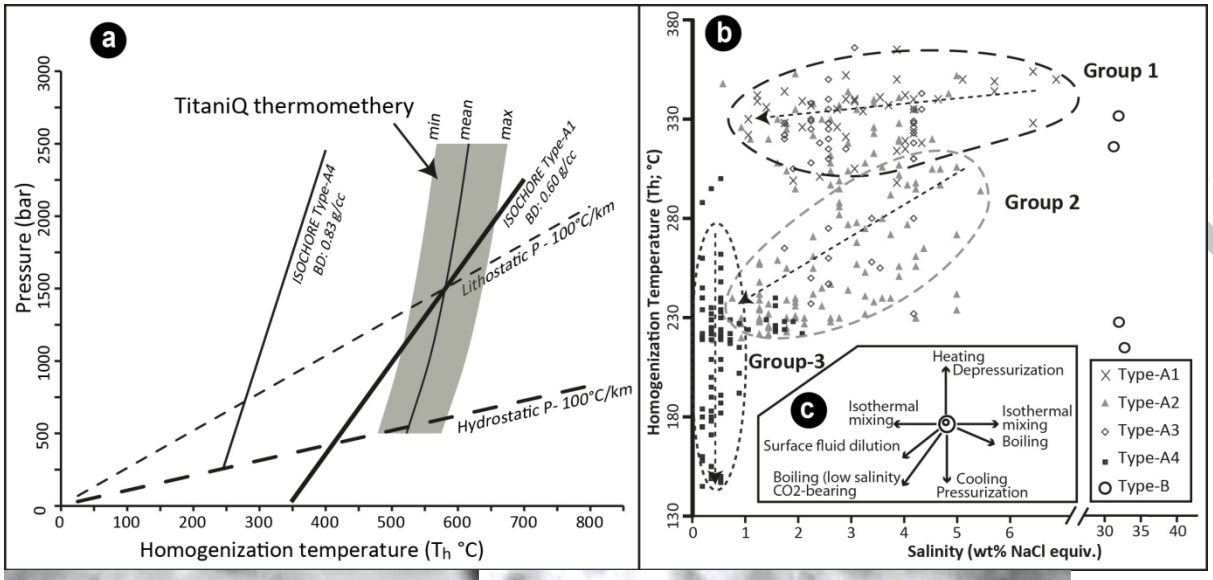
a
TitaniQ thermomethery
min
mean
max
ISOCHORE Type-A4
BD: 0.83 g/cc
ISOCHORE Type-A1
BD: 0.60 g/cc
Lithostatic P - 100°C/km
Hydrostatic P - 100°C/km
Pressure (bar)
Homogenization temperature (Th °C)
b
Group 1
Group 2
Group-3
Homogenization Temperature (Th; °C)
Salinity (wt% NaCl equiv.)
c
Heating
Depressurization
Isothermal mixing
Isothermal mixing
Boiling
Surface fluid dilution
Boiling (low salinity CO2-bearing
Cooling
Pressurization
Type-A1
Type-A2
Type-A3
Type-A4
Type-B

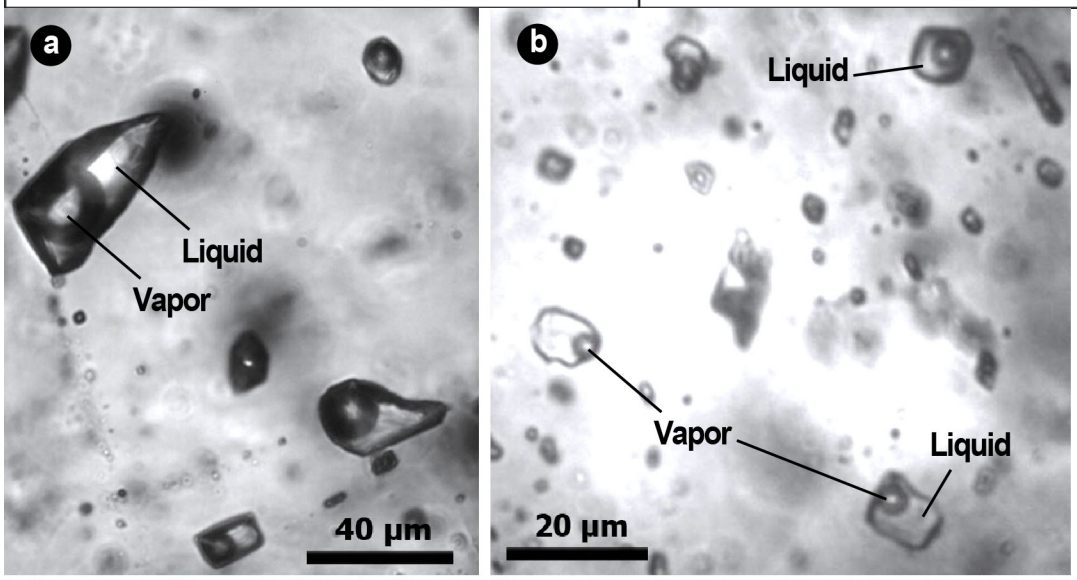
a
Liquid
Vapor
40 µm
b
Liquid
Vapor
Liquid
20 µm

1572

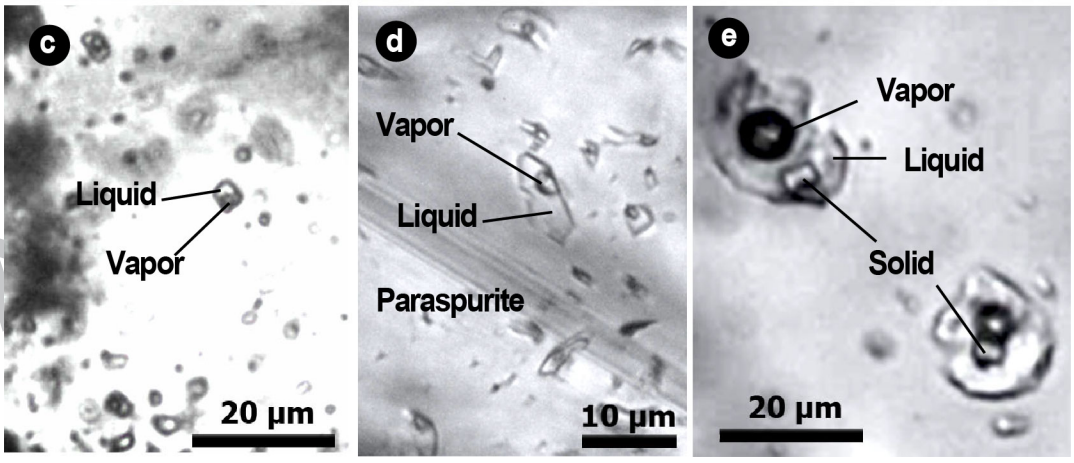
c
Liquid
Vapor
20 µm
d
Vapor
Liquid
Paraspurite
10 µm
e
Vapor
Liquid
Solid
20 µm

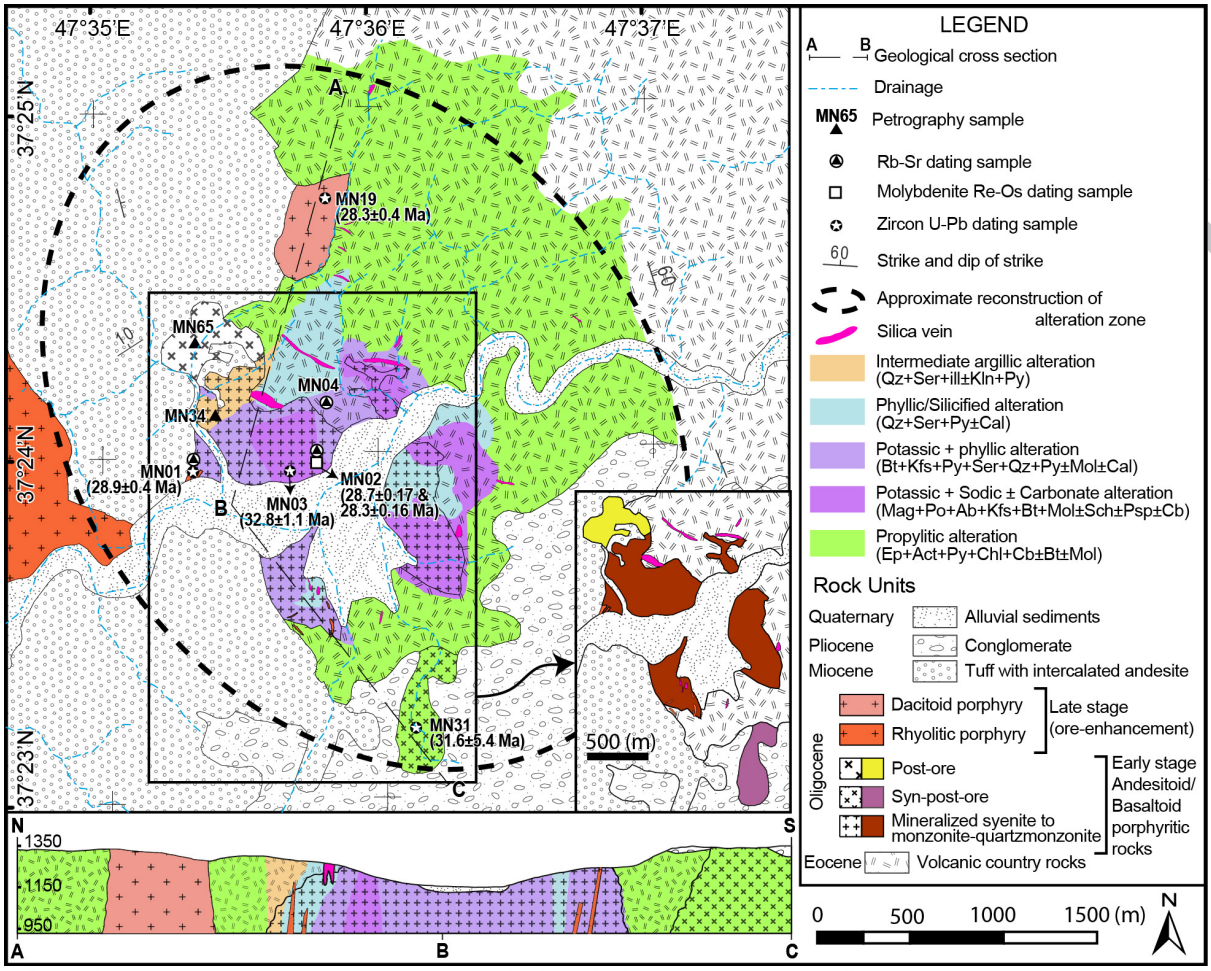
47°35'E
47°36'E
47°37'E
37°25'N
37°24'N
37°23'N
A
B
C
MN19 (28.3±0.4 Ma)
MN65
MN04
MN34
MN01 (28.9±0.4 Ma)
MN03 (32.8±1.1 Ma)
MN02 (28.7±0.17 & 28.3±0.16 Ma)
MN31 (31.6±5.4 Ma)
500 (m)
N
S
1350
1150
950
LEGEND
Geological cross section
Drainage
Petrography sample
Rb-Sr dating sample
Molybdenite Re-Os dating sample
Zircon U-Pb dating sample
Strike and dip of strike
Approximate reconstruction of alteration zone
Silica vein
Intermediate argillic alteration (Qz+Ser+ill±Kln+Py)
Phyllic/Silicified alteration (Qz+Ser+Py±Cal)
Potassic + phyllic alteration (Bt+Kfs+Py+Ser+Qz+Py±Mol±Cal)
Potassic + Sodic ± Carbonate alteration (Mag+Po+Ab+Kfs+Bt+Mol±Sch±Psp±Cb)
Propylitic alteration (Ep+Act+Py+Chl+Cb±Bt±Mol)
Rock Units
Quaternary
Pliocene
Miocene
Alluvial sediments
Conglomerate
Tuff with intercalated andesite
Oligocene
Dacitoid porphyry
Rhyolitic porphyry
Late stage (ore-enhancement)
Post-ore
Syn-post-ore
Mineralized syenite to monzonite-quartzmonzonite
Early stage Andesitoid/ Basaltoid porphyritic rocks
Eocene
Volcanic country rocks
0
500
1000
1500 (m)

1573

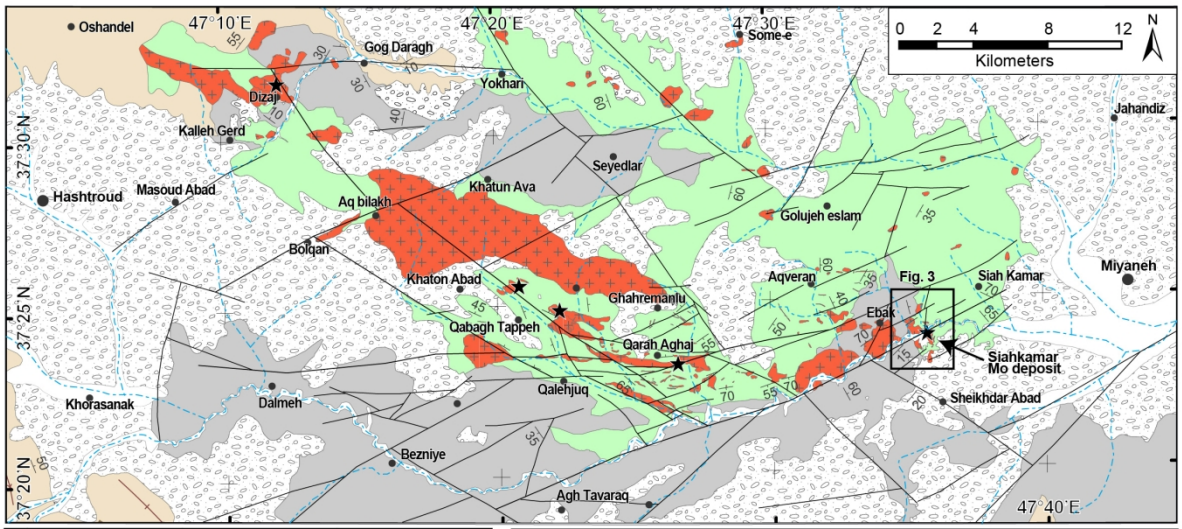
Oshandel
47°10'E
47°20'E
47°30'E
Some-e
Gog Daragh
Yokhari
Dizaj
Kalleh Gerd
Hashtroud
Masoud Abad
Aq bilakh
Khatun Ava
Seyedlar
Jahandiz
Golujeh eslam
Bolqan
Khaton Abad
Ghahremanlu
Qabagh Tappeh
Qarah Aghaj
Aqveran
Fig. 3
Siah Kamar
Miyaneh
Ebak
Siahkamar Mo deposit
Sheikhdar Abad
Khorasanak
Dalmeh
Qalehjuq
Bezniye
Agh Tavaraq
37°30'N
37°25'N
37°20'N
47°40'E
0 2 4 8 12
Kilometers
N

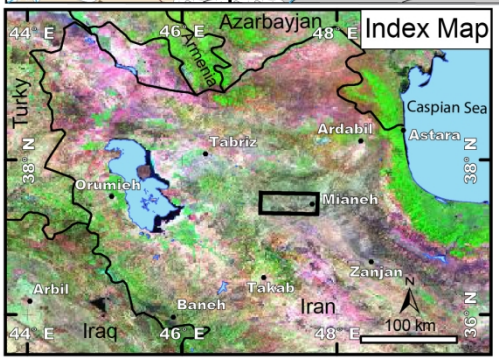
Index Map
Azarbayjan
Armenia
Turky
Caspian Sea
Ardabil
Astara
Tabriz
Orumieh
Mianeh
Zanjan
Takab
Arbil
Baneh
Iran
Iraq
100 km
44° E
46° E
48° E
38° N
36° N

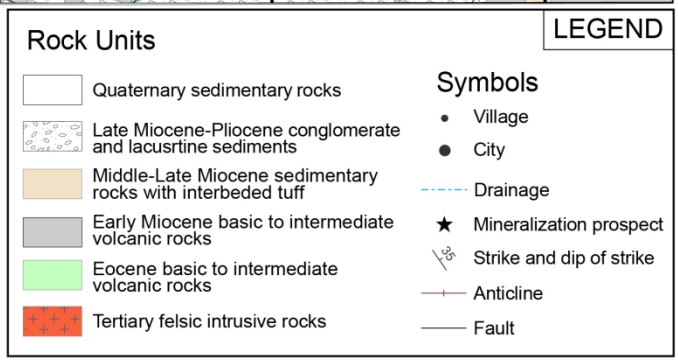
LEGEND
Rock Units
Quaternary sedimentary rocks
Late Miocene-Pliocene conglomerate and lacusrtine sediments
Middle-Late Miocene sedimentary rocks with interbeded tuff
Early Miocene basic to intermediate volcanic rocks
Eocene basic to intermediate volcanic rocks
Tertiary felsic intrusive rocks
Symbols
Village
City
Drainage
Mineralization prospect
Strike and dip of strike
Anticline
Fault

1574

1575

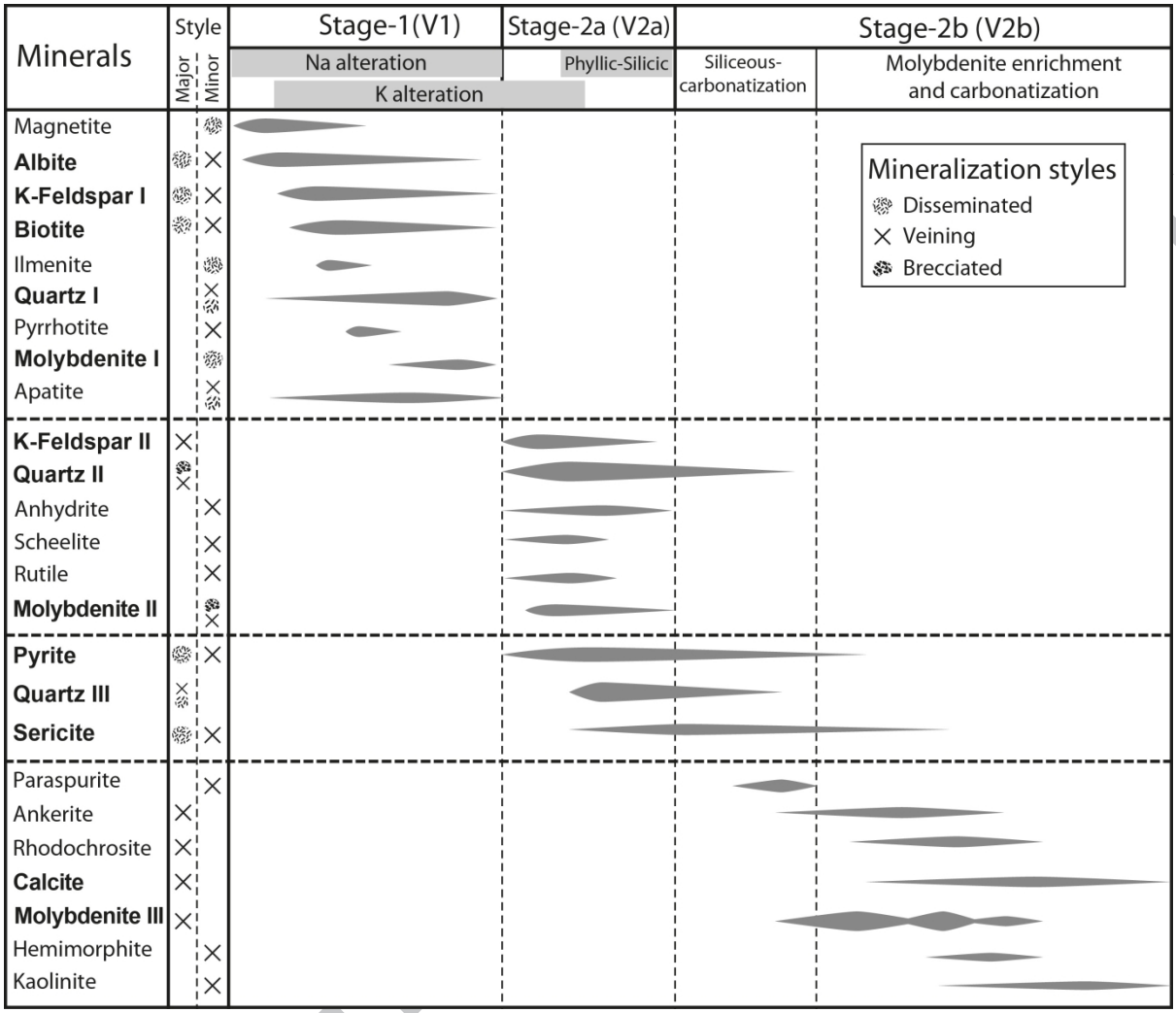

1576

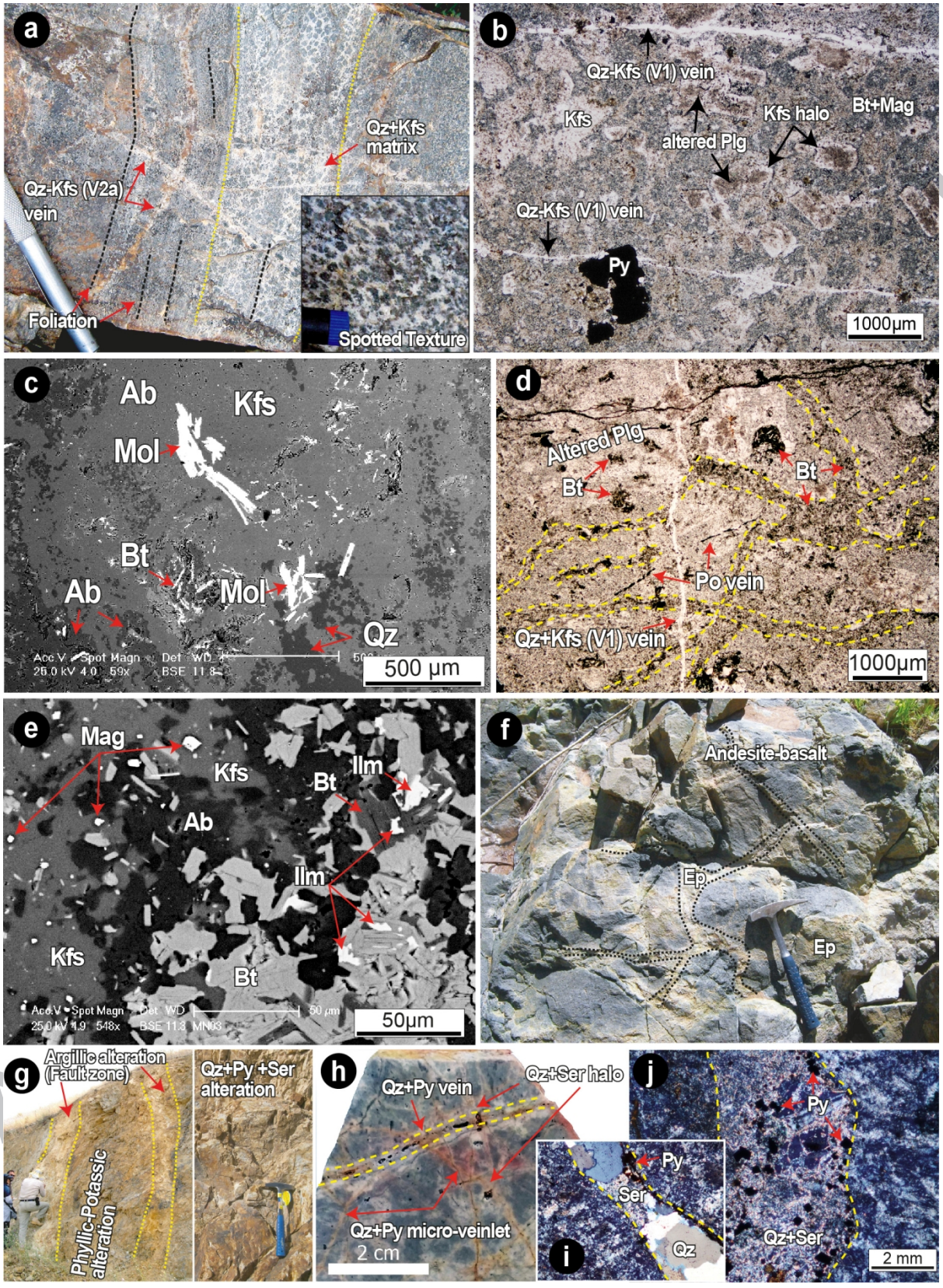
a
Qz+Kfs matrix
Qz-Kfs (V2a) vein
Foliation
Spotted Texture
b
Qz-Kfs (V1) vein
Kfs
altered Plg
Kfs halo
Bt+Mag
Qz-Kfs (V1) vein
Py
1000µm
c
Ab
Kfs
Mol
Bt
Ab
Mol
Qz
500 µm
d
Altered Plg
Bt
Bt
Po vein
Qz+Kfs (V1) vein
1000µm
e
Mag
Kfs
Bt
Ilm
Ab
Ilm
Kfs
Bt
50µm
f
Andesite-basalt
Ep
Ep
g
Argillic alteration (Fault zone)
Phyllic-Potassic alteration
Qz+Py +Ser alteration
h
Qz+Py vein
Qz+Ser halo
Qz+Py micro-veinlet
2 cm
i
Py
Ser
Qz
j
Py
Qz+Ser
2 mm

1577

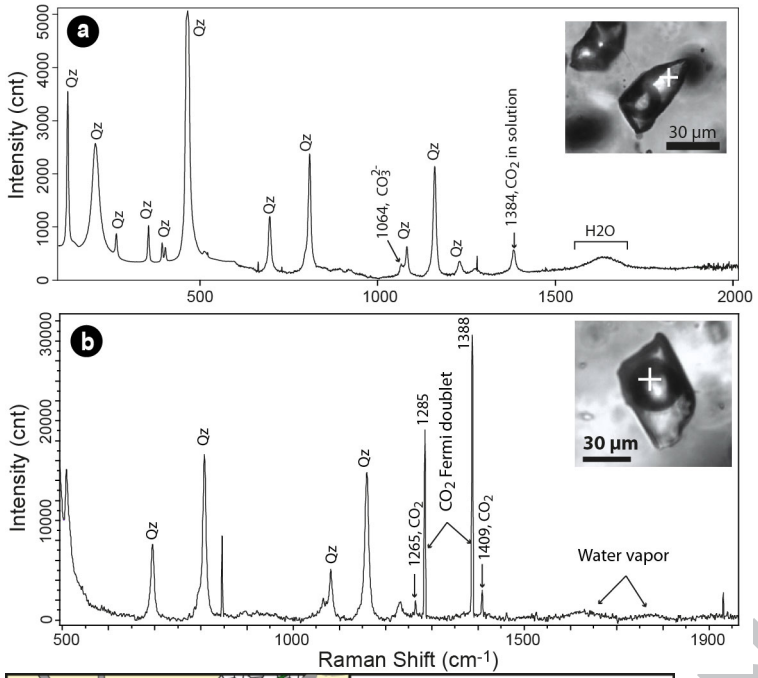

1578

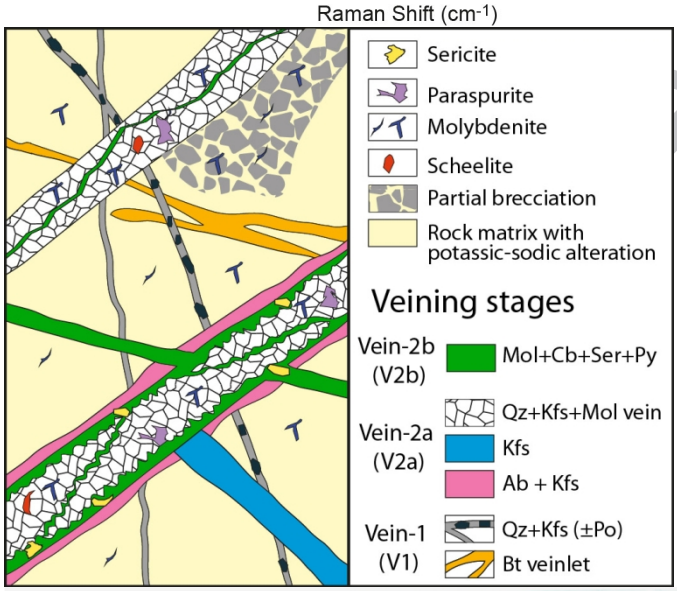

1579

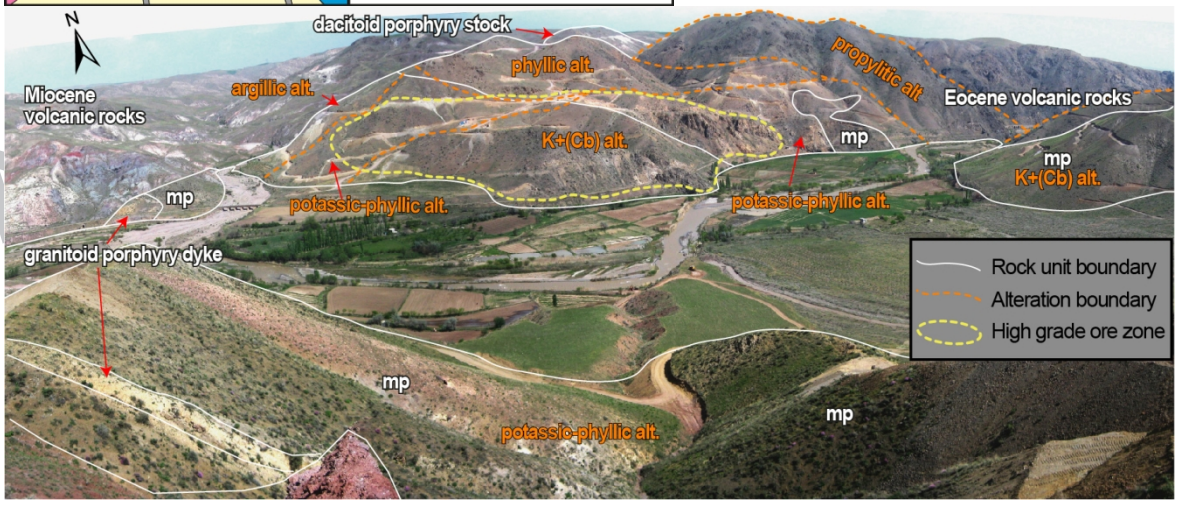

1580

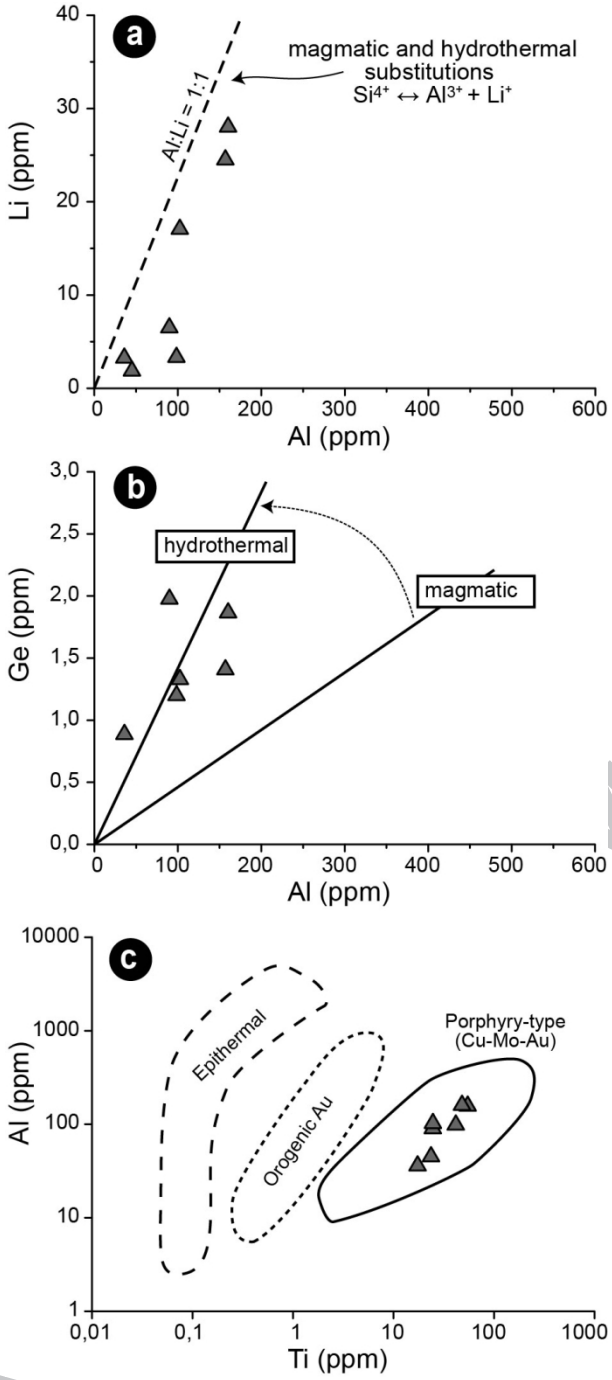

1581

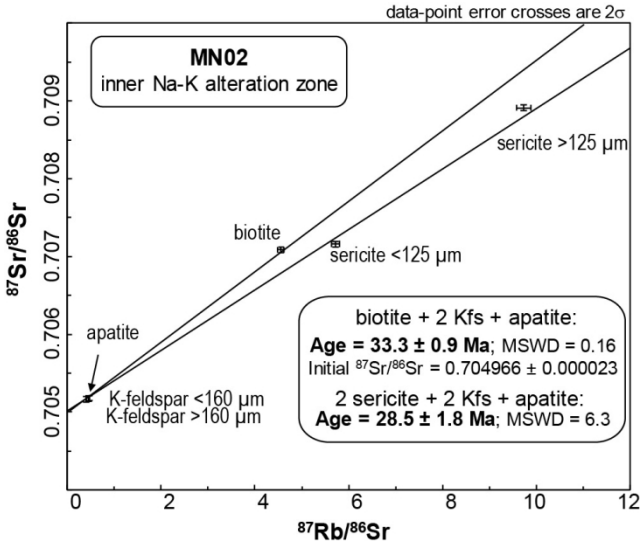
data-point error crosses are 2σ
MN02
inner Na-K alteration zone
sericite >125 µm
biotite
sericite <125 µm
apatite
K-feldspar <160 µm
K-feldspar >160 µm
biotite + 2 Kfs + apatite:
Age = 33.3 ± 0.9 Ma; MSWD = 0.16
Initial 87Sr/86Sr = 0.704966 ± 0.000023
2 sericite + 2 Kfs + apatite:
Age = 28.5 ± 1.8 Ma; MSWD = 6.3
87Sr/86Sr
87Rb/86Sr
0.705
0.706
0.707
0.708
0.709
0
2
4
6
8
10
12

1582

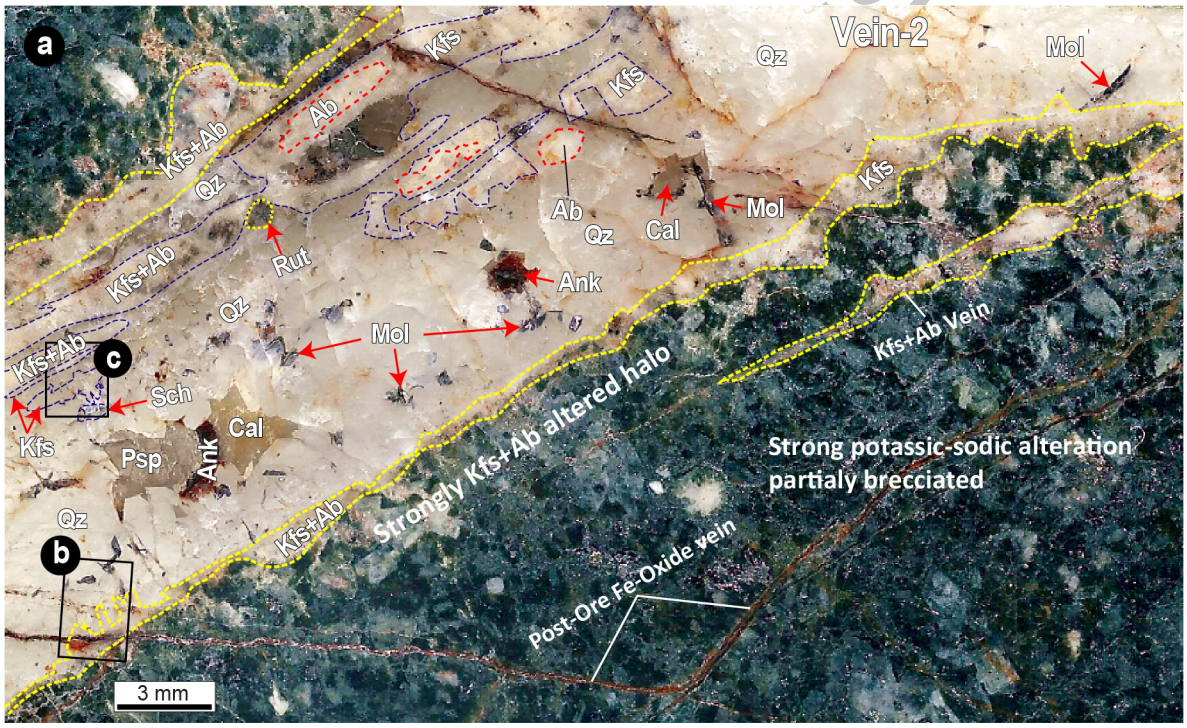
a
Vein-2
Kfs
Qz
Mol
Ab
Kfs+Ab
Qz
Rut
Ank
Cal
Sch
Psp
Ank
Strongly Kfs+Ab altered halo
Kfs+Ab Vein
Strong potassic-sodic alteration
partialy brecciated
Post-Ore Fe-Oxide vein
b
c
3 mm

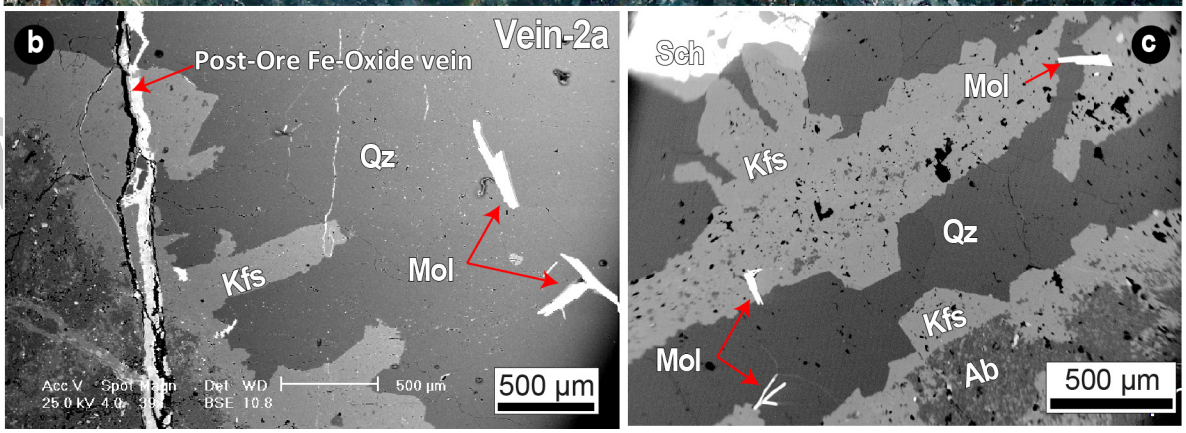
b
Vein-2a
Post-Ore Fe-Oxide vein
Qz
Kfs
Mol
500 µm
c
Sch
Mol
Kfs
Qz
Kfs
Mol
Ab
500 µm

1583

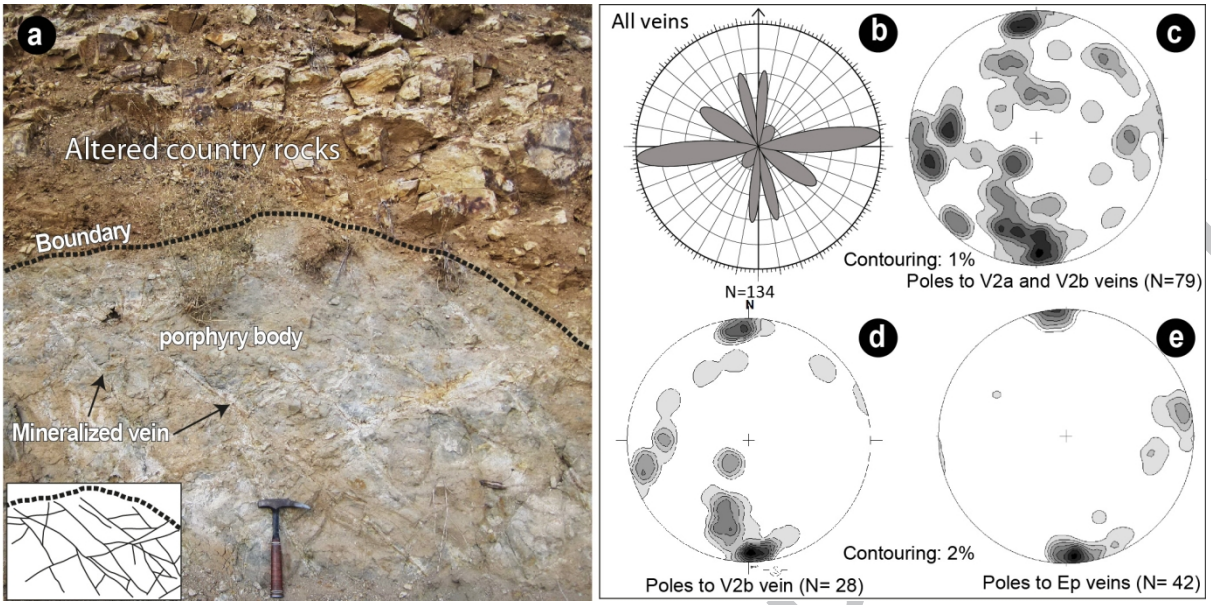

1584

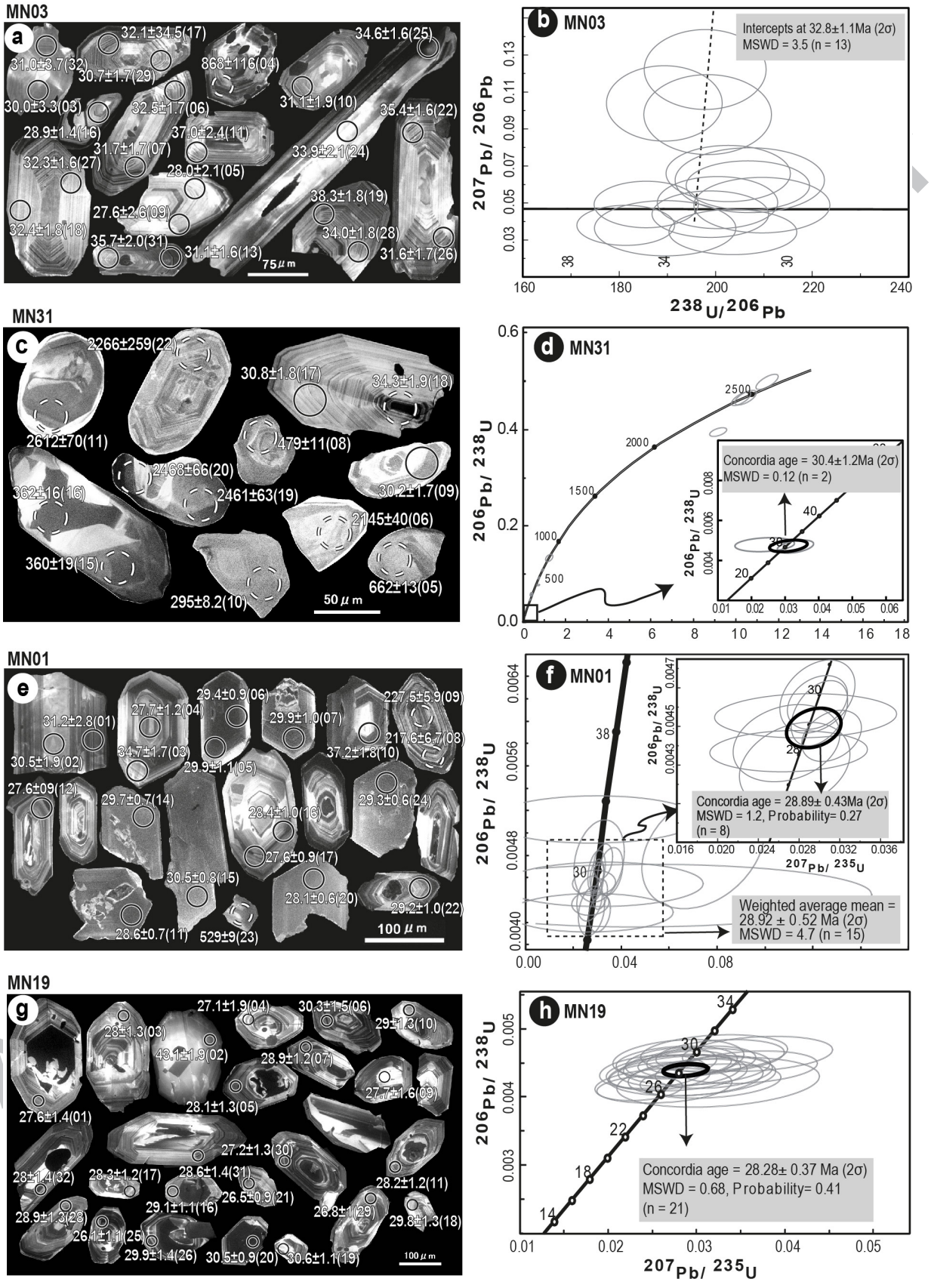
MN03
a
32.1±34.5(17)
34.6±1.6(25)
31.0±3.7(32)
30.7±1.7(29)
868±116(04)
30.0±3.3(03)
32.5±1.7(06)
31.1±1.9(10)
35.4±1.6(22)
28.9±1.4(16)
37.0±2.4(11)
31.7±1.7(07)
33.9±2.1(24)
32.3±1.6(27)
28.0±2.1(05)
38.3±1.8(19)
27.6±2.6(09)
32.4±1.8(18)
34.0±1.8(28)
35.7±2.0(31)
31.1±1.6(13)
31.6±1.7(26)
75 μm
b MN03
Intercepts at 32.8±1.1Ma (2σ)
MSWD = 3.5 (n = 13)
207Pb/ 206Pb
238U/206Pb
MN31
c
2266±259(22)
30.8±1.8(17)
34.3±1.9(18)
2612±70(11)
479±11(08)
2468±66(20)
362±16(16)
2461±63(19)
30.2±1.7(09)
2145±40(06)
360±19(15)
662±13(05)
295±8.2(10)
50 μm
d MN31
206Pb/ 238U
Concordia age = 30.4±1.2Ma (2σ)
MSWD = 0.12 (n = 2)
MN01
e
29.4±0.9(06)
227.5±5.9(09)
31.2±2.8(01)
27.7±1.2(04)
29.9±1.0(07)
217.6±6.7(08)
34.7±1.7(03)
37.2±1.8(10)
30.5±1.9(02)
29.9±1.1(05)
27.6±09(12)
29.7±0.7(14)
29.3±0.6(24)
28.4±1.0(16)
27.6±0.9(17)
30.5±0.8(15)
28.1±0.6(20)
29.2±1.0(22)
28.6±0.7(11)
529±9(23)
100 μm
f MN01
206Pb/ 238U
Concordia age = 28.89± 0.43Ma (2σ)
MSWD = 1.2, Probability= 0.27
(n = 8)
207Pb/ 235U
Weighted average mean =
28.92 ± 0.52 Ma (2σ)
MSWD = 4.7 (n = 15)
MN19
g
27.1±1.9(04)
30.3±1.5(06)
29±1.3(10)
28±1.3(03)
43.1±1.9(02)
28.9±1.2(07)
27.7±1.6(09)
27.6±1.4(01)
28.1±1.3(05)
27.2±1.3(30)
28±1.4(32)
28.3±1.2(17)
28.6±1.4(31)
28.2±1.2(11)
26.5±0.9(21)
29.1±1.1(16)
28.9±1.3(28)
26.8±1(29)
29.8±1.3(18)
26.1±1.1(25)
29.9±1.4(26)
30.5±0.9(20)
30.6±1.1(19)
100 μm
h MN19
206Pb/ 238U
Concordia age = 28.28± 0.37 Ma (2σ)
MSWD = 0.68, Probability= 0.41
(n = 21)
207Pb/ 235U

1585

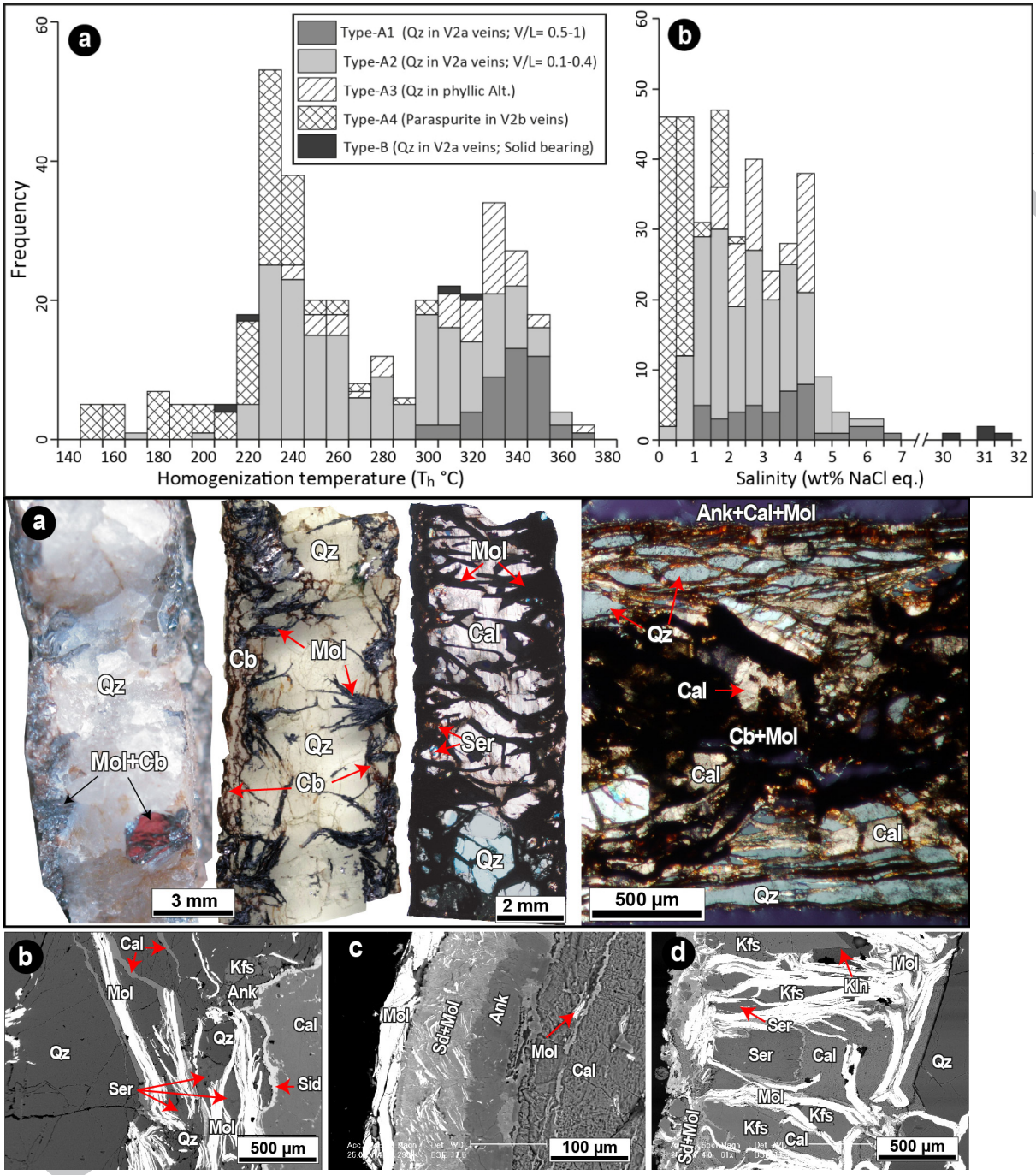

1586

1587

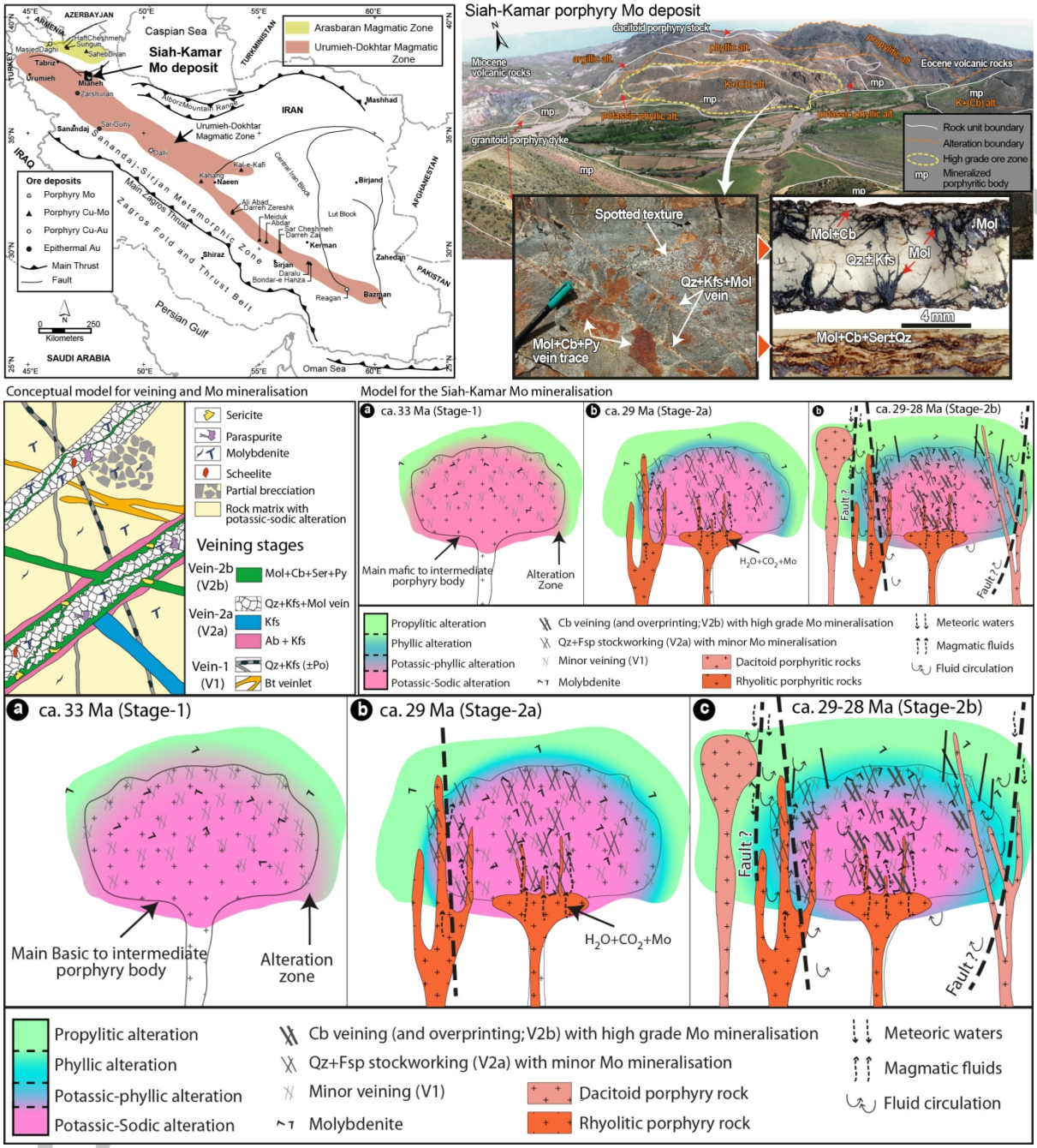

Highlights

- Long-lived magmatism and differentiation control Mo ore mineralisation
- Mo ore-enhancement caused by renewed magmatism
- Mo ore associated with carbonatisation, acidic fluid neutralisation and cooling
- Refertilised crust leading to Mo ore formation in the Urumieh-Dokhtar zone